Dry and strong quartz during deformation of the lower crust in the presence of melt

Luca Menegon,[1] Pritam Nasipuri,[1] Holger Stünitz,[1] Harald Behrens,[2] and Erling Ravna[1]

[1] Granulite facies migmatitic gneisses from the Seiland Igneous Province (northern Norway) were deformed during deep crustal shearing in the presence of melt, which formed by dehydration melting of biotite. Partial melting and deformation occurred during the intrusion of large gabbroic plutons at the base of the lower crust at 570 to 520 Ma in an intracontinental rift setting. The migmatitic gneisses consist of high-aspect-ratio leucosome-rich domains and a leucosome-poor, restitic domain of quartzitic composition. According to thermodynamic modeling using synkinematic mineral assemblages, deformation occurred at T = 760°C–820°C, P = 0.75–0.95 GPa and in the presence of ≤5 vol % of residual melt. There is direct evidence from microstructural observations, Fourier transform infrared measurements, thermodynamic modeling, and titanium-in-quartz thermometry that dry quartz in the leucosome-poor domain deformed at high differential stress (50–100 MPa) by dislocation creep. High stresses are demonstrated by the small grain size (11–17 μm) of quartz in localized layers of recrystallized grains, where titanium-in-quartz thermometry yields 770°C–815°C. Dry and strong quartz forms a load-bearing framework in the migmatitic gneisses, where ~5% melt is present, but does not control the mechanical behavior because it is located in isolated pockets. The high stress deformation of quartz overprints an earlier, lower stress deformation, which is preserved particularly in the vicinity of segregated melt pockets. The grain-scale melt distribution, water content and distribution, and the overprinting relationships of quartz microstructures indicate that biotite dehydration melting occurred during deformation by dislocation creep in quartz. The water partitioned into the segregated melt crystallizing in isolated pockets, in the vicinity of which quartz shows a higher intracrystalline water content and a large grain size. On the contrary, the leucosome-poor domain of the rock, from which melt was removed, became dry and thereby mechanically stronger. Melt removal at larger scale will result in a lower crust which is dry enough to be mechanically strong. The application of flow laws derived for wet quartz is not appropriate to estimate the behavior of such granulite facies parts of the lower crust.

Citation: Menegon, L., P. Nasipuri, H. Stünitz, H. Behrens, and E. Ravna (2011), Dry and strong quartz during deformation of the lower crust in the presence of melt, *J. Geophys. Res.*, *116*, B10410, doi:10.1029/2011JB008371.

1. Introduction

[2] The knowledge of the mechanical behavior of the lower continental crust is of equal importance to that of the middle to upper crust when the deformation along lithospheric-scale fault zones and the mechanics of major geodynamic processes are to be understood. As access to and direct observation of the lower crust are difficult, estimates of the strength of the lower crust are largely based on the inversion of geophysical and geodetic data and on the extrapolation of rock mechanics experiments to natural deformation conditions [e.g., *Kohlstedt et al.*, 1995; *Rybacki and Dresen*, 2000; *Bürgmann and Dresen*, 2008]. Laboratory-derived dislocation creep flow laws for common rock-forming minerals (quartz and plagioclase) deformed under wet conditions predict a weak lower crust with a strength of less than 30 MPa when deformed at temperature T above 700°C at geological strain rates of 10^{-12}–10^{-14} s^{-1} [*Paterson and Luan*, 1990; *Luan and Paterson*, 1992; *Gleason and Tullis*, 1995; *Hirth et al.*, 2001; *Bürgmann and Dresen*, 2008, and references therein]. Consequently, a rheological model of a weak lower crust overlying a mechanically stronger upper mantle is commonly utilized and the overall structure of many orogens and rifted margins is interpreted to depend on a major decoupling horizon, which is represented by a weak lower crust above a strong upper mantle [e.g., *Handy and Brun*, 2004].

[3] However, modeling of lithosphere rheology, observation of seismicity distribution, estimates of the effective

[1]Department of Geology, University of Tromsø, Tromsø, Norway.
[2]Institute of Mineralogy, University of Hannover, Hannover, Germany.

elastic thickness of the lithosphere, as well as the occurrence of pseudotachylytes in lower crustal rocks indicate higher stresses than those predicted from wet flow laws for typical geological strain rates of 10^{-12} to 10^{-14} s^{-1} [*Austrheim and Boundy*, 1994; *Maggi et al.*, 2000; *Jackson*, 2002; *Afonso and Ranalli*, 2004; *Jackson et al.*, 2004; *Lund et al.*, 2004; *Jackson et al.*, 2008; *Priestley et al.*, 2008]. These observations and inferences are consistent with a rheological model of a strong lower crust, most likely overlying a weaker upper mantle. The high strength of the lower crust at high temperatures of deformation likely results from large parts of this crust being dry [*Austrheim and Boundy*, 1994; *Jackson et al.*, 2004; *Fitz Gerald et al.*, 2006]. Therefore, the presence or absence of small amounts of water may be the controlling factor for the strength of the lower crust given that ambient temperatures are high [e.g., *Jackson et al.*, 2004].

[4] The study of natural shear zones and their microstructures developed in deep crustal rocks can help to shed light on the debates concerning the strength and mechanical behavior of the lower crust. Investigations of exhumed deep crustal sections as well as xenoliths indicate that large portions of the lower crust consist of felsic and mafic granulites that have equilibrated under high-grade (T > 750°C) metamorphic conditions [e.g., *Bohlen and Mezger*, 1989; *Rudnick and Fountain*, 1995; *Hacker et al.*, 2000; *Müntener et al.*, 2000]. High temperature anatexis involving dehydration melting reactions is one of the principal mechanisms to generate H_2O-undersaturated felsic melts and produce dry, residual, granulite facies mineral assemblages [e.g., *Stevens and Clemens*, 1993; *Brown*, 1994]. When dehydration melting at granulite facies conditions is accompanied by melt removal, the residual rocks are strongly H_2O depleted because the H_2O is partitioned into the silicate melts [*Brown*, 2002; *White and Powell*, 2002; *Guernina and Sawyer*, 2003]. The preservation of the high temperature dry mineral assemblages in many granulite facies terrains during their prolonged residence in the lower crust prior to uplift and exhumation has been taken by, for example, *Yardley and Valley* [1994, 1997] as petrologic evidence for large portions of the lower crust being effectively dry.

[5] The partitioning of water into the segregated melt and the subsequent melt loss are likely to have a profound rheological effect on the crystals in the residual rock, making them stronger than their "wet" equivalents [*White and Powell*, 2002]. Likewise, a hardening rather than a softening effect resulting from partial melting in the upper mantle has been inferred by *Karato* [1986], provided that the melt fraction is small and is associated with limited amounts of available water. Partial melting will deplete the water content of the olivine crystals making them strong during dislocation creep.

[6] This mechanism for producing a dry lower crust and thereby dramatically increasing its strength appears convincing, but observational evidence for its operation is partly lacking. In particular, one question deserves particular attention: Is the resulting H_2O-deficient, solid assemblage after partial melting dry enough to be mechanically strong? The H_2O content of dry, mechanically strong single crystals of quartz are on the order of 30–200 H/10^6 Si [*Kronenberg et al.*, 1986; *Kronenberg and Wolf*, 1990]. For plagioclase, high strength in dislocation creep deformation was found

for dry polycrystalline material at ~640 H/10^6 Si [*Rybacki and Dresen*, 2000]. Thus, the H_2O content of these nominally anhydrous minerals required to constitute mechanically strong behavior for dislocation creep are very low (for quartz, the H_2O content is near the estimated maximum solubility of molecular H_2O, less than 100 H/10^6 Si [*Gerretsen et al.*, 1989], whereas the maximum H_2O content for feldspar is unknown, but probably somewhat higher than that for quartz).

[7] In this paper, we report a microstructural and petrologic investigation of felsic granulites from the Seiland Igneous Province in northern Norway. The granulite facies metamorphism is accompanied by partial melting and shear deformation in an intracontinental rifting environment. The intrusion of large gabbroic plutons at the base of the lower crust provided the heat source for the high temperature metamorphism and partial melting [*Elvevold et al.*, 1994]. The granulites contain up to 75 vol % of quartz, which controls their strength. Such a high percentage of quartz allows the rheology of the rock to be estimated quite well, because existing piezometers and flow laws [e.g., *Hirth et al.*, 2001; *Stipp and Tullis*, 2003; *Shimizu*, 2008] can be applied.

2. Geological Setting

[8] The Seiland Igneous Province (SIP) of the north Norwegian Caledonides (Figure 1) consists of a deep-seated alkaline magmatic suite of dominantly gabbroic composition [e.g., *Krill and Zwaan*, 1987; *Elvevold et al.*, 1994; *Roberts et al.*, 2006]. The intrusives were emplaced during the time span from 570 to 520 Ma [*Roberts et al.*, 2006] into two tectonostratigraphically distinct units [*Rice*, 1990; *Elvevold et al.*, 1994]. The upper unit consists of metasediments of the Sørøy Group, and the lower unit is composed of high-grade paragneisses of the Eidvågeid Sequence. Field relationships, geochemical, and geochronological constraints indicate that the SIP was emplaced in an intracontinental rift setting, most likely related to the incipient stages of opening of the Iapetus Ocean [*Krill and Zwaan*, 1987; *Elvevold et al.*, 1994; *Reginiussen et al.*, 1995; *Roberts et al.*, 2006].

[9] During the intrusions, the host rocks were contact metamorphosed at peak conditions of T = 930°C–960°C and P = 0.55–0.7 GPa, and subsequently recrystallized and cooled to intermediate-pressure granulite facies conditions (700°C–750°C and 0.5–0.7 GPa) [*Elvevold et al.*, 1994]. Contact metamorphism and granulite facies re-equilibration were accompanied by the development of a penetrative gneissic to mylonitic foliation in both the mafic rocks and the metasediments. The granulite facies foliation forms the dominant structure over large portions of the SIP; it dips steeply (>60°) to WSW and contains a stretching lineation plunging steeply to moderately to NW. Asymmetric fabrics (e.g., porphyroclast systems, C′-type shear bands) indicate that the sense of shear was top-down-to-NW (Figure 2a). The solid-state foliation is parallel to a primary magmatic banding locally preserved in the gabbros and defined by the rhythmic alternation of centimeter-thick to decimeter-thick leucocratic and mafic layers. The parallelism between the magmatic layering and the solid-state foliation has been taken as indicative of synintrusive deep crustal shearing
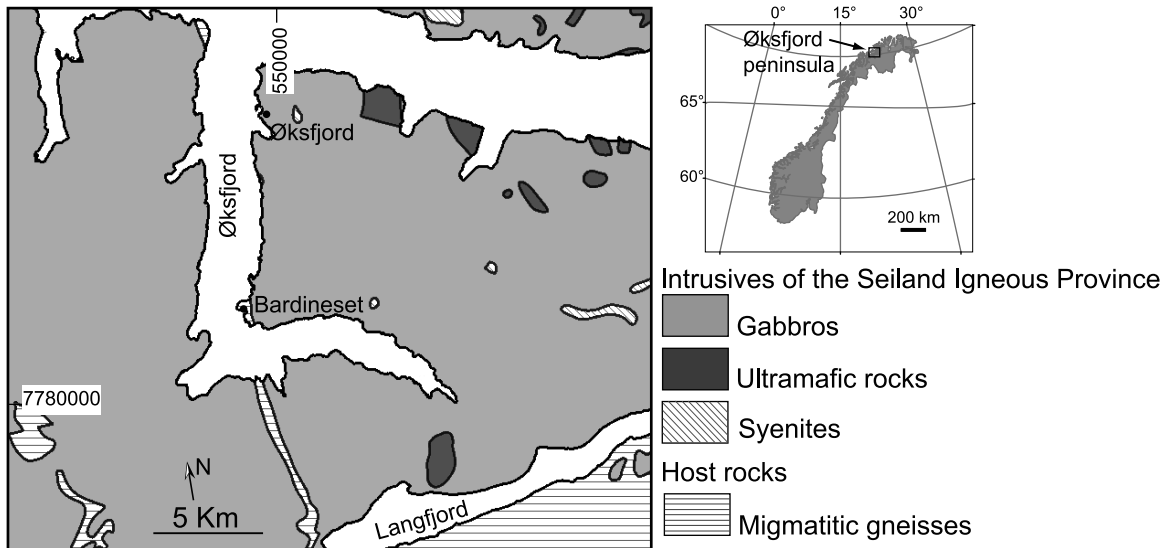
Figure 1. Simplified geological map of the Seiland Igneous Province in the Øksfjord Peninsula. Modified after *Roberts* [1973].

during lithospheric extension [*Elvevold et al.*, 1994], and this interpretation is supported by the same radiometric age obtained by *Roberts et al.* [2006] from undeformed and strongly sheared rocks of the SIP. Although the SIP forms a part of the Kalak Nappe Complex in the Middle Allochthon of the north Norwegian Caledonides [*Kirkland et al.*, 2008, and references therein], it has largely escaped the Caledonian tectono-metamorphic overprint, and the granulite facies assemblage is well preserved throughout the SIP.

3. Methods of Study

[10] The petrography and microstructure of the samples have been studied by polarized light and scanning electron microscopy (SEM) on polished thin sections cut normal to the foliation and parallel to the stretching lineation. SEM backscattered electron images were collected on a Philips XL-30-ESEM-FEG at the Department of Geological Sciences, Stockholm University, and on a Jeol-840 SEM at the Department of Medical Biology, University of Tromsø. Digital image analysis using Image SXM (http://www.liv.ac.uk/~sdb/ImageSXM/) on SEM backscattered electron micrographs was performed to evaluate phase proportion and distribution.

[11] The quartz crystallographic preferred orientation (CPO) and the size of dynamically recrystallized quartz grains were measured by (1) electron backscatter diffraction (EBSD) [*Adams et al.*, 1992] and (2) computer-integrated polarization microscopy (CIP) [*Panozzo-Heilbronner and Pauli*, 1993]. EBSD analysis was performed with a Philips XL-30-ESEM-FEG at the Department of Geological Sciences, Stockholm University. Working conditions during the acqui-
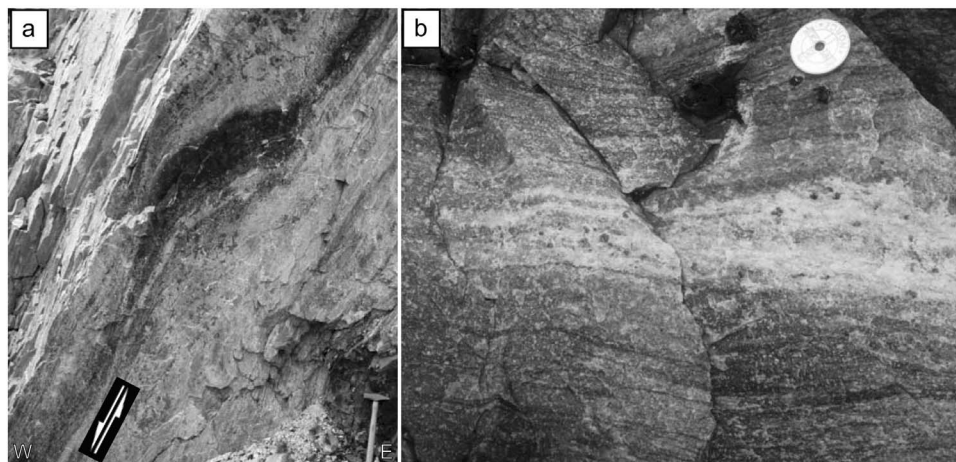

Figure 2. The migmatitic gneisses from the Bardineset locality. (a) Sheared mafic dyke in the migmatitic gneisses, indicating top-to-NW sense of shear; hammer (40 cm long) for scale. (b) Stromatic migmatite characterized by garnet-rich leucosomes elongated parallel to the tectonic foliation and by a quartz-rich restite portion (greyish in the picture); coin (1.6 cm diameter) for scale.
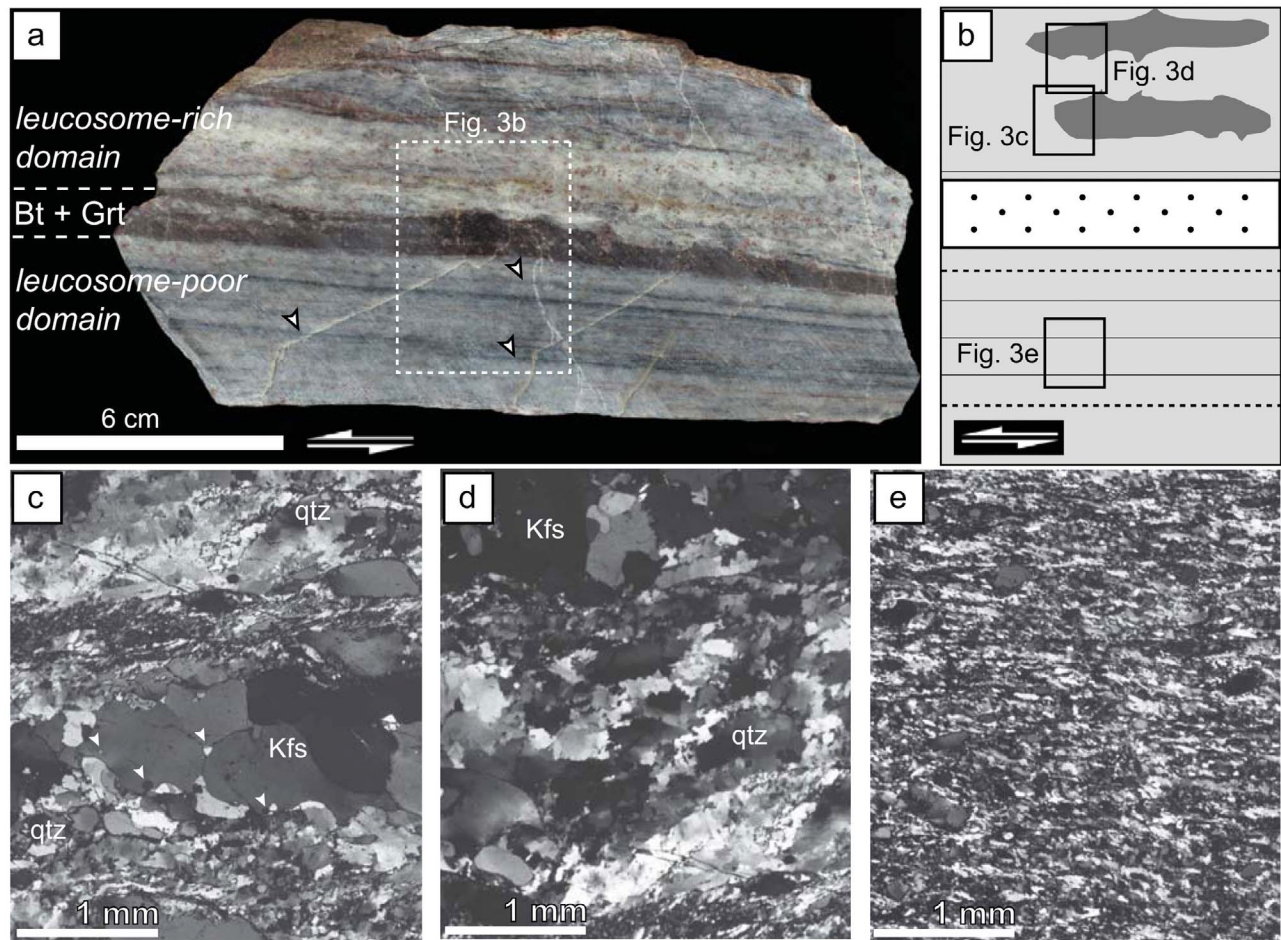
Figure 3. (a) Representative sample of the deformed migmatites (sample Ø15). The well-developed mylonitic foliation and the lack of elongate patches of leucosomes occur in the leucosome-poor domain (lower part). Arrowheads indicate some fine-grained ultramylonite layers parallel to the mylonitic foliation. The dashed white rectangle denotes the area sketched in Figure 3b. (b) Schematic line drawings of the migmatite sample investigated. The light grey background represents the quartzitic layers, whereas the dark grey lenses represent the high aspect ratio leucosomes in the leucosome-rich domain. Thin black lines mark the trace of the mylonitic foliation, the dashed black lines that of fine-grained ultramylonite layers. The dotted area represents a biotite-rich + garnet-rich layer. Rectangles denote the areas shown in Figures 3c, 3d, and 3e. (c) Light micrograph of an elliptical patch of leucosome elongate on the foliation. White arrowheads indicate rounded inclusions of quartz and plagioclase within large grains of K-feldspar; crossed polarizers. (d) Representative quartz microstructure in the leucosome-rich domain, characterized by large grain and subgrain sizes and by coarsely sutured grain boundaries. (e) Representative quartz microstructure in the leucosome-poor domain, characterized by polycrystalline ribbons of finer recrystallized grains with a shape preferred orientation consistent with the sinistral sense of shear.

sition of the EBSD patterns were: 20 kV accelerating voltage, ~0.8 nA beam current, working distance of ~17 mm, 70° sample tilt, and low-vacuum mode (0.2–0.3 torr). EBSD patterns were indexed using Channel 5 software from HKL Technology, Oxford Instruments. The analysis of grain size distribution was performed on the recrystallized grains automatically identified by the indexing software when completely surrounded by boundaries with misorientation angles >10°. The photomicrographs processed by the CIP method were acquired with an Optronics MicroFire monochrome digital camera on a Zeiss-Jena polarization microscope at the Department of Geology, Tromsø University, with magnifications ranging from 3.2X to 25X. For each analyzed site, a *c* axis pole figure and a color-coded *c* axis orientation image were calculated, which portrays the quartz *c* axis orientation at every pixel of the image. To measure the size of dynamically recrystallized quartz grains in the ultramylonite layers, grain boundary maps were produced by manually digitizing grain boundaries on *c* axis orientation images and by using the Lazy Grain Boundary method [*Heilbronner*, 2000]. In both the EBSD- and CIP-derived measurements, the grain size of each grain was calculated as the diameter of the circle with an area equivalent to that of the grain.

[12] Major element oxide abundances of the leucosome-rich and leucosome-poor domains of sample Ø15 (Figures 2b

and 3a) were determined by XRF analysis. Powder samples were produced from ~6 mm thick slices of the two domains with a tungsten carbide ball mill. Sample pellets were prepared from the powders and analyzed with a Philips MagiX-PRO PW2440 X-ray spectrometer at the National Geophysical Research Institute, Hyderabad, India. Analytical precision was ±0.02 wt %.

[13] Chemical compositions of minerals were determined using a four wavelength dispersive spectrometer, JEOL Superprobe electron-probe micro analyzer (EPMA) at the GeoCenter, Copenhagen, Denmark. Working conditions were: accelerating voltage 15 kV, sample current 15 nA, and beam diameter 1 μm. Natural and synthetic silicates and oxides were used for standardization. Different analytical conditions were used for measuring the Ti concentration in quartz. Ti content (in ppm by weight) is measured simultaneously in three spectrometers, with an accelerating voltage of 20 kV, sample current of 30 nA, and beam diameter range of 2–5 μm, depending on the grain size of quartz. Rutile was used as the internal standard for standardization. Detection limit using three spectrometers was 10 ppm.

[14] Fourier transform infrared (FTIR) spectroscopy was used to measure the total content of water-related species within individual quartz grains. A thick section encompassing the leucosome-rich and leucosome-poor domains of sample Ø15 (Figure 3a) was cut from the same chip of the one used for preparation of a standard thin section for petrographic and microstructural observations. The average thickness of the section (167 μm) was measured with a digital micrometer with a precision of ±2 μm. Spectra were recorded at room temperature in the range 600–6000 cm^{-1} using an IR microscope (IR scope II) attached to a Bruker IFS88 FTIR spectrometer at the Institute of Mineralogy, University of Hannover, Germany. A globar light source, a KBr beam splitter, and a MCT narrow range detector were used. Fifty scans per spectrum were accumulated with a spectral resolution of 2 cm^{-1}. A slit aperture between the objective and the detector was used to limit the analyzed sample volume. In the focus plane, the area selected by the slit was 50 μm × 50 μm.

4. Results

4.1. Sample Description: Granulite Facies Migmatites

[15] All data presented here come from granulite facies migmatitic gneisses sampled on the Øksfjord peninsula in the southeastern part of the Seiland Igneous Province (GPS coordinates relative to World Geodetic System 84, zone 34 W, 0549420 East, 7783845 North; Figures 1 and 2). The rocks described here come from a major belt of migmatites in the Bardineset locality (Figure 1). On the basis of field appearance and petrographic features, *Elvevold et al.* [1994] speculated that the protolith of the migmatitic gneisses in Bardineset was the high-grade (migmatitic) paragneiss of the Eidvågeid Sequence, occurring within the Kalak nappe complex some tens of kilometers to the NE of the Seiland Igneous Province. However, given the high degree of partial melting in the Bardineset migmatites and their marked restitic character, the actual nature and composition of the protolith cannot be unequivocally determined.

[16] The Bardineset migmatitic gneisses occur in relatively small lenticular enclaves in the metagabbros, ranging

in thickness from a few meters to several tens of meters, and in a major NNW-SSE-trending belt, about 1 km in width (Figure 1). Partial melting is developed at all scales, resulting in the formation of stromatic migmatites with leucosomes forming high-aspect-ratio domains parallel to the foliation of the sheared rock (Figures 2b and 3a). Thin section microstructures (see later in the text) indicate that partial melting was synkinematic to the deformation.

[17] The migmatites show a distinct compositional banding parallel to the foliation, with several centimeter-thick, leucosome-rich domains alternating with leucosome-poor domains of dominantly quartzitic composition. The latter show a thickness of several decimeters and a well-developed mylonitic foliation. The high aspect ratio leucosomes are generally sinuous in shape and contain garnet (Figures 2b and 3a). Up to 1–2 cm thick biotite + garnet-rich layers (Figure 3a) are also locally present along the foliation.

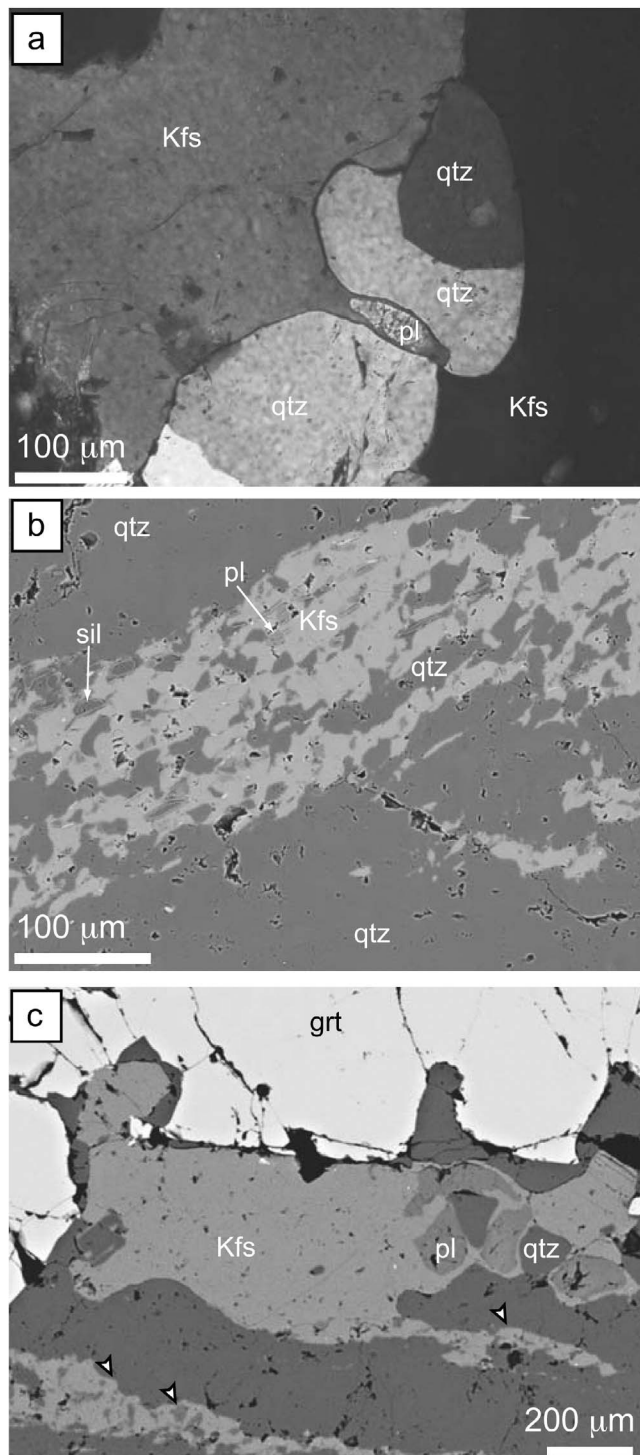### 4.2. Petrography, Reaction Microstructures, and Grain-Scale Melt Distribution

[18] The deformed migmatites consist of quartz, K-feldspar, garnet, sillimanite, plagioclase, biotite, ilmenite ± rutile. The granulite facies assemblage is well preserved and no evidence for late, low-temperature retrograde reactions (e.g., white mica replacing sillimanite) has been observed. At the thin section scale, the leucosome-rich domains contain up to 1–2 cm long lenses of leucosome embedded in a quartzitic matrix and concordant with the foliation (Figures 3b and 3c). The leucosome-poor domain does not contain these large leucosomes and dominantly consists of polycrystalline ribbons of quartz (Figure 3b). One distinctive feature of the studied samples is the occurrence of thin (≤500 μm thick) zones characterized by extensive grain size reduction and an ultramylonitic fabric. They only occur in the leucosome-poor, quartzitic layers as arrays of planar structures (spaced ~1−2 cm apart) parallel to the mylonitic foliation (Figures 3a and 3b).

[19] As the microstructure of quartz in the leucosome-rich, leucosome-poor, and the ultramylonite domains varies significantly (Figures 3c–3e), it is described separately in section 4.3. The reaction microstructures and the mineral assemblage do not change in the three domains. In order to highlight the differences in the amount and distribution of partial melt, the three domains will be described separately in the following sections. According to criteria reviewed by *Holness and Clemens* [1999], *Sawyer* [1999, 2001], *Marchildon and Brown* [2002], and *Holness and Sawyer* [2008], we use the following microstructures as indicative of the presence of former melt: (1) cuspate-lobate boundaries of minerals replacing pockets inferred to be pools of crystallized melts; (2) irregularly shaped pockets containing rounded and corroded reactant minerals surrounded by crystallized melt, and/or small euhedral grains grown from melt; (3) monomineralic melt films along grain boundaries; and (4) small (<60°) 2-D apparent dihedral angles between grains, indicative of small equilibrium dihedral angles between siliceous melt and solid.

4.2.1. Leucosome-Rich Domains
[20] The leucosome dominantly consists of coarse-grained (up to 1–2 mm), anhedral K-feldspar grains with rounded inclusions of quartz and plagioclase. Small quartz grains are locally present at triple junctions between K-feldspar grains

(Figure 3c). The large K-feldspar grains typically show a cuspate and lobate outline to the adjacent quartz in the restite matrix (Figure 3c). Cuspate extensions grade into thin (less than 10 μm) monomineralic films of K-feldspar along quartz-quartz grain boundaries and quartz-plagioclase or quartz-sillimanite phase boundaries (Figure 4a). Minerals in the leucosome appear optically strain free, and only a weak undulatory extinction has locally been observed in K-feldspar.

[21] In addition to the large lenses of leucosome, the foliation contains up to 200 μm thick, discontinuous "microgranitoid" patches and stringers, with an average composition of ~70 vol % K-feldspar, ~25 vol % quartz, and ~5 vol % plagioclase (Figure 4b). Quartz and plagioclase are entirely surrounded by K-feldspar and show both rounded and, to a minor extent, euhedral shape. Many of these patches also show cuspate extensions toward the residual quartz in the matrix, and contain fragmented and corroded needles of sillimanite (Figure 4b).

[22] Garnet occurs as up to 0.5 cm large porphyroblasts containing abundant rounded and lobate inclusions of quartz; less common inclusions are of sillimanite, biotite, plagioclase, rutile and ilmenite. Garnet grains are typically embayed by cuspate and lobate K-feldspar-rich domains including up to 200 μm large rounded grains of plagioclase and quartz (Figure 4c). These domains have elongate and tapered K-feldspar-rich extensions containing small ($\leq$50 μm) grains of quartz and plagioclase, which form discontinuous stringers parallel to the foliation (Figure 4c).

[23] Biotite occurs as rare skeletal grains closely associated with the garnet porphyroblasts and as fine-grained (~10–30 μm long) lamellae along discontinuous, anastomosing folia. Rutile and ilmenite are rare and usually occur as inclusions within porphyroblasts of garnet.

4.2.2. Leucosome-Poor Domains

[24] The leucosome-poor domains show a well-developed mylonitic fabric with polycrystalline ribbons of quartz (up to 75 vol %) and porphyroclasts of K-feldspar, sillimanite, and garnet. Stromatic leucosomes of high aspect ratio with large K-feldspar grains do not occur in these quartzitic layers. Only microgranitoid stringers, equivalent to those observed in the leucosome-rich domains, are common. They are up to 100–200 μm thick and form isolated patches elongated parallel to the mylonitic foliation. In these patches, sillimanite needles as well as quartz and plagioclase grains are surrounded by K-feldspar (Figure 5a).

[25] Sillimanite also occurs outside the K-feldspar-rich patches as up to 1 mm long mineral fishes, synthetic with the shear sense (Figure 5b). The sillimanite fishes are invariably rimmed by thin monomineralic K-feldspar-rich melt films. The melt films are thicker in asymmetric strain shadows (Figure 5b).

[26] As in the leucosome-rich domain, garnet is typically embayed by irregularly shaped K-feldspar-rich melt pools

Figure 4. Microstructure of the leucosome-rich domain; foliation is horizontal in all pictures. (a) Detail of a large K-feldspar grain in the leucosome showing a cuspate extension along grain boundaries of rounded quartz grains. The extension entirely rims a small elliptical grain of plagioclase; crossed polarizer. (b) SEM backscattered electron (BSE) image of an elongate patch of K-feldspar-rich "microgranitoid" between matrix quartz grains. Note the lack of K-feldspar films along quartz-quartz grain boundaries in the matrix and along intra and intercrystalline fractures. (c) SEM-BSE image of a K-feldspar-rich pool embaying a garnet porphyroblast. Note the irregular shape of the pool and the extensions grading to stringers of microgranitoid, indicated by the arrowheads. Mineral abbreviations: Kfs = K-feldspar, qtz = quartz, pl = plagioclase, sil = sillimanite, grt = garnet.
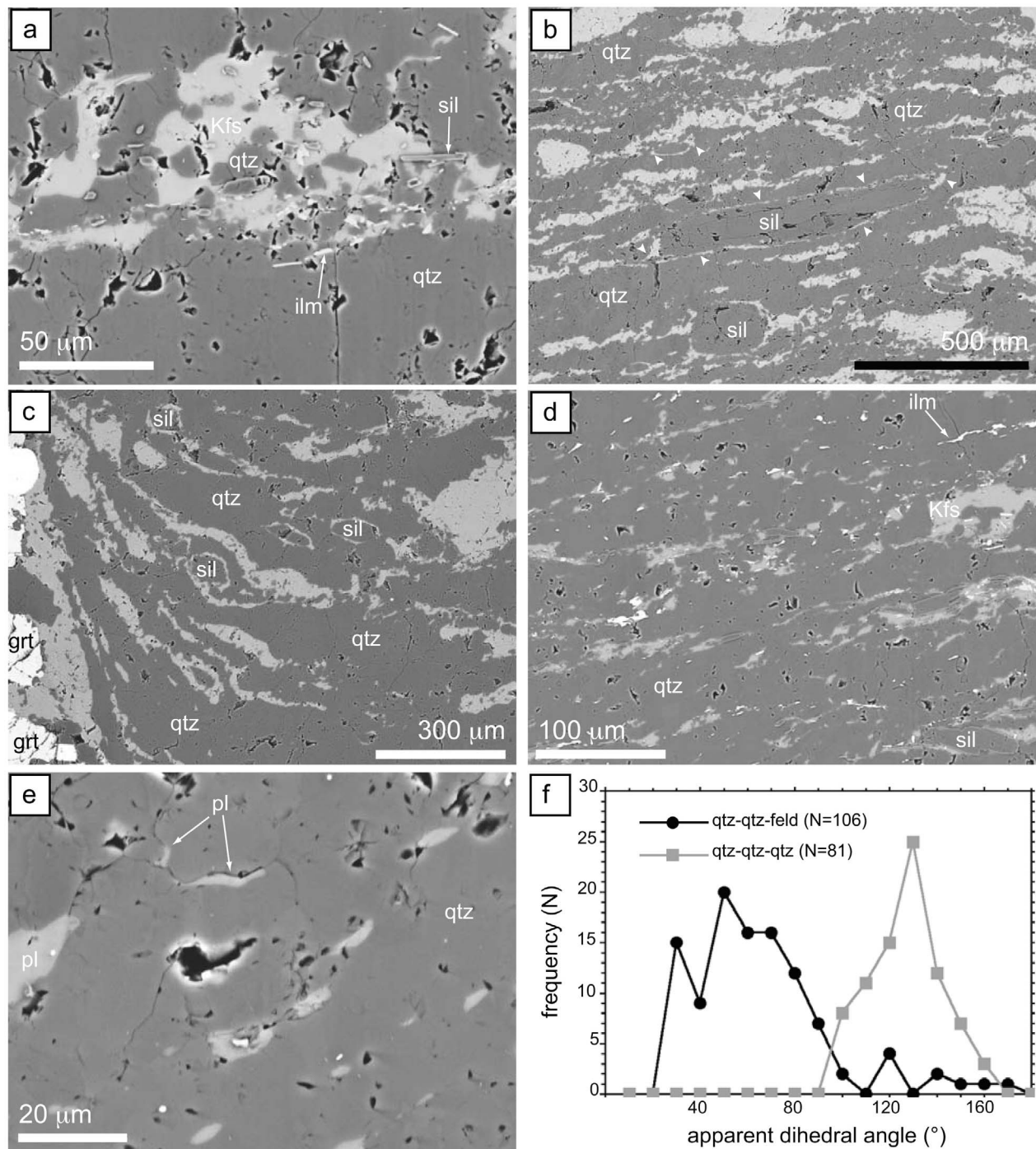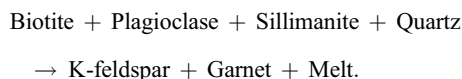
Figure 5. SEM-BSE images of (a–c) the leucosome-poor domain and (d–e) the ultramylonite layers. The mylonitic and ultramylonitic foliations are horizontal in all pictures. (a) Irregular-shaped K-feldspar-rich patch along the mylonitic foliation. (b) Asymmetric mineral fish of sillimanite indicating dextral shear sense and rimmed by a melt film of K-feldspar (white arrowheads). (c) Microgranitoid stringers extending from an embayment around a garnet porphyroblast. Sillimanite grains are rimmed by K-feldspar films. (d) Microstructure of an ultramylonite layer. Quartz forms about 75 vol % of the layer. (e) Thin plagioclase films and beads along quartz grain boundaries and at triple junctions between quartz grains. (f) Distribution of the 2-D apparent dihedral angle between mineral grain triple junctions (quartz-quartz-quartz and quartz-quartz-feldspars) in the ultramylonite layers. The peak of quartz triple junctions apparent dihedral angles is well defined (median of 120°), whereas the quartz-quartz-feldspars apparent angles have a broad maximum between 30° and 80° (median 54°). *N* is the number of measured apparent angles. Mineral abbreviations: Kfs = K-feldspar, qtz = quartz, grt = garnet, pl = plagioclase, sil = sillimanite, ilm = ilmenite.

locally containing quartz, plagioclase, and sillimanite. The melt pools grade into the discontinuous microgranitoid stringers along the mylonitic foliation (Figure 5c). Inclusions in garnet are mostly of rounded and lobate quartz, along with minor biotite, sillimanite, and plagioclase.

[27] Biotite is subordinate and is distributed locally along thin, discontinuous folia. It is very fine grained ($\leq$10 μm in length) and associated with minor ilmenite.

[28] In summary, the spatial association of minerals in the leucosome, the corroded quartz in the quartzitic layers, the mineral inclusions in the garnet, and the K-feldspar-rich domains embaying garnet are all indicative of the following biotite dehydration melting reaction [e.g., *Le Breton and Thompson*, 1988; *White et al.*, 2007]

$$\text{Biotite} + \text{Plagioclase} + \text{Sillimanite} + \text{Quartz}$$

$$\rightarrow \text{K-feldspar} + \text{Garnet} + \text{Melt}.$$

K-feldspar occurs both as a peritectic mineral and as the main component of the melt fraction. The quartz-rich layers are interpreted to be the restite left after the removal of most of the melt from the protolith, and the stromatic leucosomes represent products of the segregated melt.

4.2.3. Fine-Grained Ultramylonite Layers

[29] The ultramylonite layers are less than 500 μm wide and consist of more than 80 vol % of fine-grained, dynamically recrystallized quartz (see section 4.3.3.), with minor amounts of K-feldspar + plagioclase + sillimanite $\pm$ biotite $\pm$ ilmenite (Figure 5d). K-feldspar-rich melt occurs in irregularly shaped pockets, variably elongated along the foliation and up to 70–100 μm in length. The pockets can either be essentially monomineralic (K-feldspar) or may, additionally, contain plagioclase, quartz, and sillimanite. A minor amount of similar irregularly shaped pockets dominantly consists of plagioclase. K-feldspar (and, to a lesser extent, plagioclase) locally occurs as thin (<5 μm thick), monomineralic films along some quartz grain boundaries and as small grains at the triple junctions between quartz grains (Figure 5e). Pockets and films typically are isolated and never form an interconnected framework. The cumulative amount of pockets and films in the ultramylonite layers determined from image analysis is ~8 vol %. However, given that K-feldspar also occurs as solid product of the dehydration melting reaction, image analysis most likely results in an overestimate of the melt amount.

[30] The apparent dihedral angle distribution measured at the triple junctions between plagioclase-quartz-quartz and K-feldspar-quartz-quartz grains shows a broad peak at around 60°, with a median value of 54°. In contrast, the dihedral angle distribution of quartz triple junctions shows a peak between 100° and 150°, with a median value of 120° (Figure 5f). The low dihedral angles between feldspar and quartz are consistent with a feldspar melt between quartz grains as apparent interfacial angles between solid quartz and feldspars typically are above 100° [*Vernon*, 1968].

4.3. Quartz Microstructure and Crystallographic Preferred Orientation

4.3.1. Leucosome-Rich Domains

[31] In the leucosome-rich domains quartz occurs as large (hundreds of micrometers to less than 1 mm) grains.

Locally, a shape preferred orientation (SPO) is developed, which is inclined synthetically with the sense of shear. Most of the grain boundaries are coarsely lobate, and dissection microstructures, indicative of a tight interfingering of grains in three dimensions, are evident.

[32] In the light microscope the deformation microstructures of quartz include patchy to undulatory extinction, misorientation bands, subgrains, and a fine (a few micrometers in size) bulging of the grain boundaries transitional to thin aggregates of recrystallized grains about 10–20 μm in size (Figures 6a and 6b). We have observed three main types of subgrains. The first type consists of coarse (100–200 μm average size) subgrains arranged in a chessboard pattern of rectangular to square shape (Figures 6a and 6b), where the subgrain boundaries are parallel to the basal and to the prism planes. The occurrence of a chessboard subgrain pattern is limited to grains with their c axes oriented normal to the foliation, which is the dominant crystallographic orientation of quartz in the leucosome-rich domain (Figure 6c). The second type of subgrain is less common and consists of lenticular subgrains elongate subparallel to the foliation plane. Grains showing this subgrain type have their c axis oriented subparallel to the lineation and the subgrain boundaries are therefore prism boundaries (Figure 6b). The third type of subgrain is smaller in size (<20 μm) and occurs behind the bulges on both sides of a migrating boundary (Figure 6b).

4.3.2. Leucosome-Poor Domains

[33] In leucosome-poor domains, quartz occurs in monomineralic polycrystalline ribbons along the mylonitic foliation, from 500 μm to 1–2 mm wide and several centimeters long. Ribbon-forming grains range in size from ~80 μm to 400–500 μm and are preferentially elongated at an angle of 20°–30° to the foliation plane, measured synthetically with respect to the shear sense (Figure 7a). The large variation in grain size results from progressive grain size reduction by dynamic recrystallization as a combination of subgrain rotation and bulging recrystallization (Figures 7b–7d). Small grain sizes produced by bulging typically occur in localized narrow shear zones (500 μm wide), which developed after the formation of the large grains with coarsely sutured lobate grain boundaries. Localization of later, fine-grained shear zones occurs parallel to the main fabric defined by coarser grains. The later overprint by bulging recrystallization may also occur locally without planar shear zones (Figures 6a, 6b, 7c, and 7d).

[34] Unlike the leucosome-rich domain, the subgrains never show chessboard patterns and are finer in size (<80 μm) (Figures 7a–7d). Dissection microstructures have not been observed. The grain boundaries are commonly sutured on a fine scale due to the pervasive development of fine-grained bulges (10–20 μm; Figures 7a–7c). Compared to the leucosome-rich domains, later overprint produces an increased proportion of fine aggregates of recrystallized grains by bulging recrystallization. The EBSD map in Figure 7d was obtained from an area adjacent to that of Figure 7b, showing the progressive grain size reduction of quartz toward an ultramylonite layer via the extensive development of subgrains, bulges, and recrystallized grains (Figure 7c). The grains in Figure 7d are preferentially oriented with their c axes at a high angle to the foliation and with one ⟨a⟩ axis parallel to the stretching lineation (Figure 7e). This dominant

CPO of quartz in the leucosome-poor domain is very similar to that of the leucosome-rich domain.

[35] The mapped area consists of a few large (>60 μm) grains showing the pervasive development of equant to slightly lenticular subgrains, up to a few tens of microns in size. About 25% of the 338 detected grains range in size from 20 to 90 μm, comparable to the size of the subgrains in

the larger grains. These grains show smaller subgrains of the same size as bulges along the grain boundaries (10–20 μm). These bulges produce the transition to small recrystallized grains forming elongated pockets along sutured grain boundaries (Figures 7c and 7d). They form the majority of the detected grains (about 75%) and are smaller than 20 μm (average 16.8 μm, median 11 μm) (Figure 7f).

4.3.3. Fine-Grained Ultramylonite Layers

[36] Ultramylonite layers represent thin shear zones parallel to the main fabric. Recrystallized quartz grains in the ultramylonite layers have an average aspect ratio of 2.4 and a SPO with grain long axes oriented at 20°–30° to the foliation plane, with a consistent synthetic inclination with respect to the sense of shear (Figure 8a). Recrystallization is pervasive and only scattered relics of larger (40–80 μm) unrecrystallized grains are preserved. The c axis CPO of the recrystallized grains in the ultramylonite layers does not differ significantly from that of the larger grains in the leucosome-rich and leucosome-poor domains. The c axes define a strong maximum subnormal to the foliation and rotated with the sense of shear (Figure 8b).

[37] About 80% of the measured recrystallized grains ($N = 656$) are smaller than 20 μm (Figure 8c), with a mean grain size of 15.6 μm and a median value of 11.6 μm. This size is on the same order of magnitude as the recrystallized grains along sutured grain contacts in the leucosome-rich and leucosome-poor domains (Figures 6b and 7f). Using the recrystallized grain size piezometer for quartz as calibrated by *Stipp and Tullis* [2003], a grain size of 11–17 μm yields differential stresses of 70–100 MPa during dynamic recrystallization in dislocation creep. The same values are obtained using the piezometer of *Shimizu* [2008]. Differential stresses of 52–73 MPa are obtained using the calibration of *Holyoke and Kronenberg* [2010].
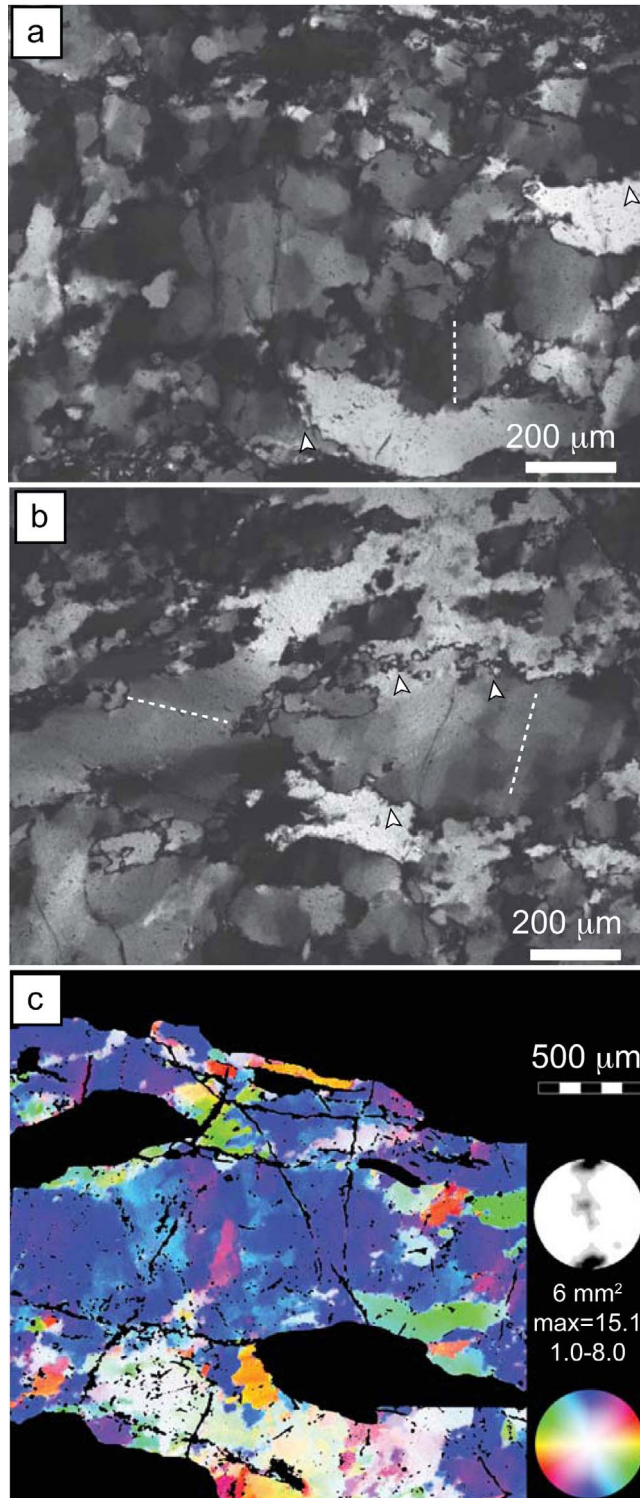
Figure 6. Microstructures and c axis crystallographic preferred orientation of quartz in the leucosome-rich domain. The foliation is horizontal. In Figures 6a and 6b, the dashed white line indicates the trace of the quartz c axis. In all the micrographs the shear sense is dextral, as established from independent shear sense indicators, and corresponds to the top-to-NW sense of shear observed on the field (Figure 2a). (a) Coarse-grained quartz with local development of coarse subgrains with a chessboard pattern. Arrowheads indicate examples of fine bulges of the grain boundaries; crossed polarizer. (b) Occurrence of elongate subgrains subparallel to the foliation plane in a grain with the c axis at a low angle to the foliation, in contrast to the occurrence of subgrains arranged in a chessboard pattern in a grain oriented with the c axis at a high angle to the foliation plane. Note the pervasive development of bulges of grain boundaries, grading to fine-grained recrystallized aggregates (see arrowheads); crossed polarizer. (c) Representative CIP-derived quartz c axis orientation image and c axis pole figure (upper hemisphere of the stereographic projection). Maximum and shading intervals at $n = 1$ time uniform are given below the pole figure. The region is 6 mm^2 and corresponds approximately to the area shown in Figure 6a. A color look-up inset is in the bottom right corner.
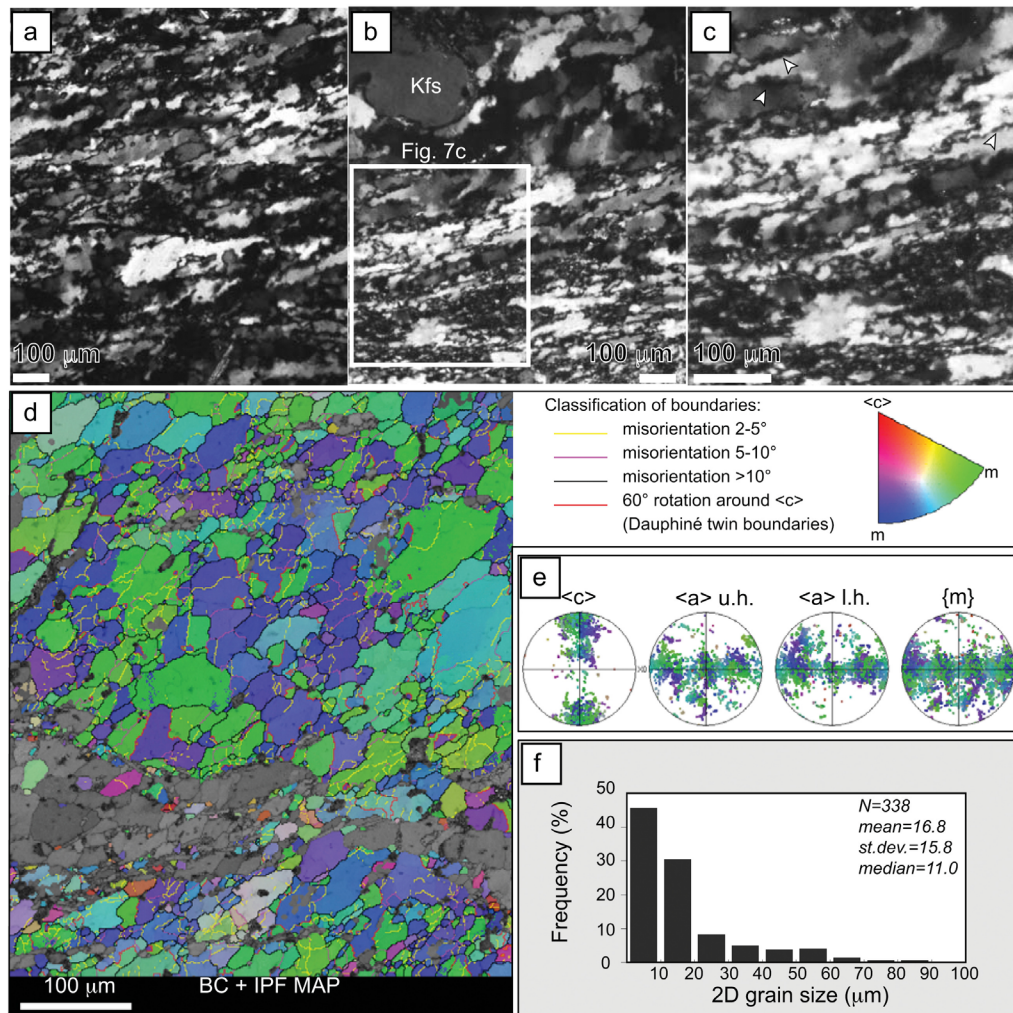
Figure 7. (a) Microstructures of quartz in the leucosome-poor, quartz-rich mylonite. The grains have an oblique shape fabric consistent with the dextral sense of shear. The grain boundaries are sutured by small bulges; crossed polarizers. (b) Microstructure of quartz showing the transition to a fine-grained ultramylonite layer in the leucosome-poor domain. The white rectangle encompasses the area shown in Figure 7c. (c) The grain size reduction of quartz to dynamically recrystallized fine grains occurs by bulging recrystallization at sutured grain boundaries (see arrowheads); crossed polarizers. (d) Processed EBSD Band Contrast (BC) + Inverse Pole Figure (IPF) map of a portion of the same microstructural transition shown in Figure 7b. EBSD data were acquired on rectangular grids by moving the electron beam at a regular step size of 1.2 μm, resulting in 99,611 data points. Grey areas are nonindexed points. The map is color coded according to the inverse pole figure for quartz shown in the upper right corner of Figure 7d, representing the crystal orientation relative to the stretching lineation of the sample (X direction). Also shown in the upper right corner of Figure 7d is the key to color code of the different boundary types. (e) Pole figures of the crystallographic orientation data for Figure 7d. Upper hemisphere, equal angle stereographic projection of the orientation of the $\langle c \rangle$ axis, $\langle a \rangle$ axis (upper and lower hemispheres, u.h., and l.h., respectively) and of the $\{m\}$ prism; color coding as in Figure 7d. (f) EBSD-derived grain size distribution of the grains detected in Figure 7d. Only grains surrounded by at least two neighbor grains have been considered. Number of measurements (N), mean value, standard deviation and median value are indicated.

4.4. Determination of P, T Conditions During Deformation

4.4.1. P, T, and X Thermodynamic Modeling

[38] P-T pseudosection analysis [*Holland and Powell*, 1998; *White et al.*, 2001; *Connolly*, 2005] is a convenient tool to understand phase topological and compositional relations for the bulk composition of the rock under con-sideration. In the present study, the primary aim of this analysis was to determine the P and T conditions at which the fine-grained aggregates of recrystallized quartz devel-oped in the leucosome-poor domain. Therefore, we have determined the TiNCKFMASH phase topological relation to explain the reaction microstructures using the bulk composition of the leucosome-poor domain (Figure 9). The
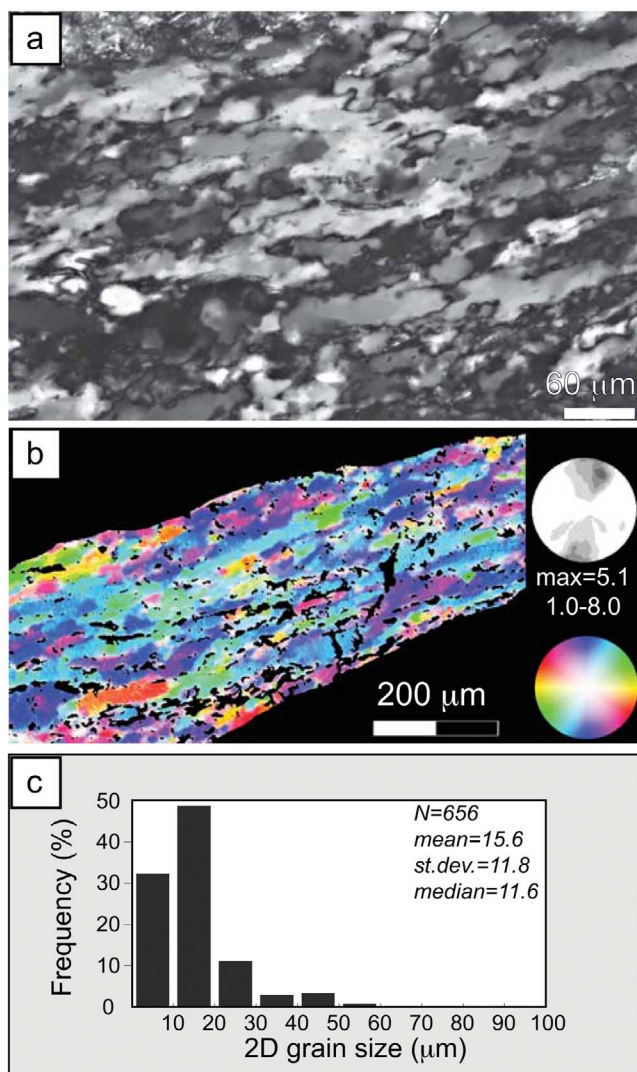
Figure 8. (a) Microstructure of quartz in the fine-grained ultramylonite layers. Most of the grains have a relatively high (>2) aspect ratio and show an oblique shape fabric, synthetic with the dextral sense of shear; crossed polarizer. (b) Representative CIP-derived quartz c axis orientation image and c axis pole figure (upper hemisphere of the stereographic projection). The grains show a CPO with a sharp maximum oriented near the Z direction of finite strain and rotated with the dextral sense of shear. Maximum and shading intervals are given below the pole figure. The color look-up table is indicated on the bottom right corner. (c) CIP-derived grain size distribution of recrystallized quartz grains from the ultramylonite layers. Number of measurements (N), mean value, standard deviation and median value are indicated.

phase diagram involves the following minerals and solution models: garnet (Grt, HP), orthopyroxene (Opx, HP), biotite (TiBio, WPH), mica (Mica, CH₂), plagioclase (Pl, h), cordierite (hCrd,), spinel (Sp, HP) and melt (HP). All the calculations were performed in Perple_X 07 [*Connolly*, 2005] using hp02ver.dat as the thermodynamic database and solut_08.dat as the solution model definition file.
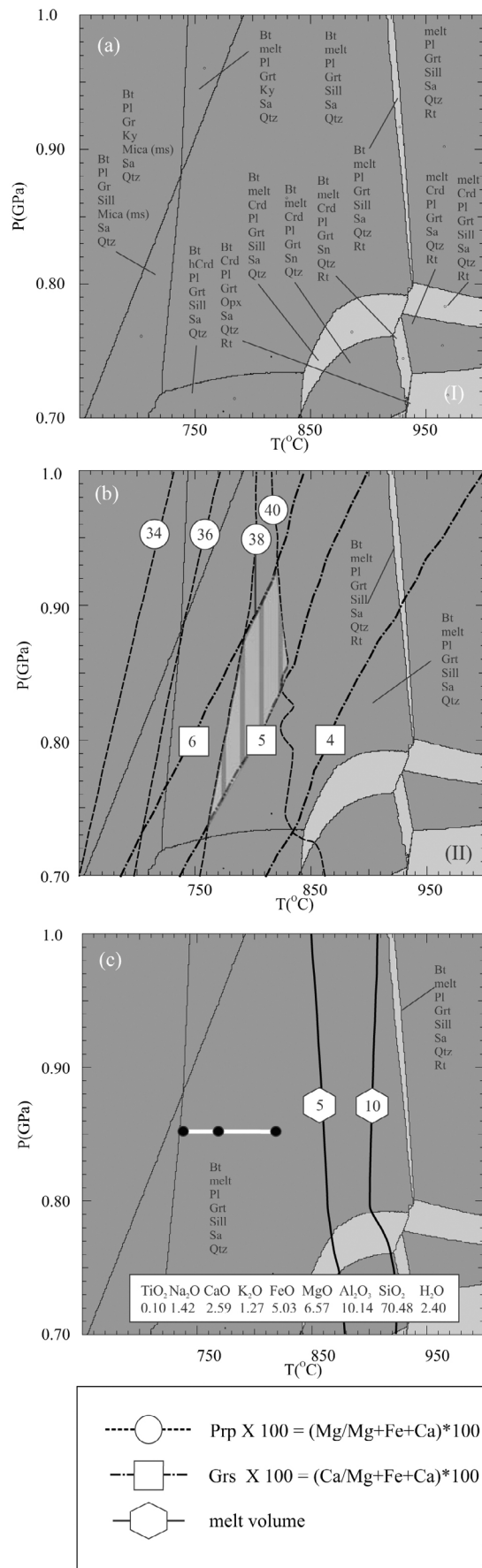
[39] The role of H_2O during the dehydration melting of biotite + quartz + plagioclase to produce garnet + plagioclase + melt is described by, for example, *Le Breton and Thompson* [1988], *Patino Douce and Beard* [1994], and *Gardien et al.* [2000]. *White et al.* [2007] discussed the effect of melt loss during progressive melting of biotite + quartz + plagioclase and preservation of garnet-bearing leucosomes. Although the $T-X(H_2O)$ pseudosection is a practical tool to describe the amount of water during dehydration melting of biotite, the constraint to estimate the amount of water for the present samples is an inhomogeneous distribution of biotite and the lack of suitable assemblages for geobarometric (Grt-Bt-Pl-Qtz and Grt-Bt-Sill-Qtz) calculations.

[40] An indirect approach is taken to estimate the water content during dehydration melting of biotite. The H_2O content is initially estimated as the difference between the ideal (100%) total and the measured total weight percent of all oxides of the representative sample Ø15 (Figure 3a and Table 1). P, T pseudosections are constructed in the TiNCKFMASH system after adjusting CaO (CaO − $3.3XP_2O_5$) and FeO (FeO+MnO) (Figure 9). Compositional isopleths of Grt (Pyrope = 100 X (Mg/Mg+Fe+Ca); Grossular = 100 X (Ca/Mg+Fe+Ca)) were plotted into the assemblage Bt + melt + Grt + Pl + Sill + San + Qtz to determine the P, T locations where the minerals have the same composition as obtained from electron microprobe analysis (Table 2). The predicted mineral compositions of Bt and Grt in the assemblage Bt + melt + Grt + Pl + Sill + San + Qtz and the measured mineral compositions do not match well. Biotite is the only mineral in the present system that can hold a significant amount of water and the amount of melt generated is dependent on the amount of biotite taking part in the dehydration reaction. Therefore, in the next step, the water content is reduced by a small amount (0.01 mol %) with respect to the previously used water content and the same operation was performed, unless the predicted mineralogical composition in the P, T pseudosection corresponds closely with the electron microprobe analysis. The compositional isopleths representative of the leucosome-poor domains are Prp_{38-40} and Grs_{05-06} (Table 2 and Figure 9).

[41] The P, T pseudosections with modified H_2O content (Figure 9) estimate P, T conditions of 760°C–820°C, 0.75–0.90 GPa (H_2O content = 0.69 wt %, normalized to 100). At these conditions, about 5 vol % of the residual melt is expected to be present in the leucosome-poor domain. It is noticeable that, at the estimated P, T conditions, the synkinematic mineral assemblage for the bulk composition of the leucosome-rich domain (Table 1) is stable only at a higher H_2O content (1.26 wt %, normalized to 100). The estimated H_2O content is slightly lower than the initial H_2O content (determined as 100% less the sum of total weight % of all oxides). The difference is 0.57% for the leucosome-rich domain and 0.92% for the leucosome-poor domain. The difference (<1%) is attributed to either an analytical error or to the influence of local effective reaction volume [*Nasipuri et al.*, 2009; *Thompson*, 1959], which is below the sampling volume of bulk rock for the present study.

4.4.2. Titanium-in-Quartz Thermometry

[42] A precise estimate of the deformation temperature is potentially possible by means of the titanium-in-quartz (TitaniQ) [*Wark and Watson*, 2006; *Kohn and Northrup*,

2009] geothermometer, using syndeformationally recrystallized grains. The applicability of TitaniQ depends on the assumption of activity of TiO_2 [Wark and Watson, 2006]. Using activity of $TiO_2 = 1$ will yield only a minimum temperature for rutile-undersaturated assemblages. In the Bardineset deformed migmatites, rutile occurs rarely, either as inclusions within garnet or in close association with rare skeletal biotite. Rutile does not occur along the foliation, suggesting that the deforming rocks were rutile undersaturated. Activity of TiO_2 in crustal rocks ranges from 0.5 to 1.0 [Ghent and Stout, 1984; Thomas et al., 2010] and was estimated to be ≥ 0.7 in metapelitic rocks on the basis of ilmenite + garnet + Al_2SiO_5 + quartz equilibria [Ghent and Stout, 1984]. Given the presence of ilmenite along the foliation, we consider $a_{TiO_2} = 0.7$ as representative for our samples. We report the TitaniQ analysis for an activity of TiO_2 of 1, 0.7 and 0.5. The results obtained for $a_{TiO_2} = 0.7$ are the most likely deformation temperatures, and those using $a_{TiO_2} = 1$ and 0.5 are considered as the minimum and maximum deformation temperatures, respectively. We have used the calibration of Thomas et al. [2010] at P = 0.85 GPa, which is established as the mean pressure estimate from the pseudosection calculation.

[43] Measurements have been collected on grains along the foliation in the leucosome-rich, leucosome-poor, and ultramylonite domains. The results for these three microstructural domains are presented separately (Table 3). One problem during the analysis of Ti-in-quartz is the damage of quartz in the electron beam. In order to avoid decreasing count rates during the measurement, the electron beam has been spread to 2–3 μm in order to yield constant count statistics for Ti over extended periods of time. Great care was taken to avoid measuring in close proximity to grain boundaries, cracks, and Ti-bearing phases as those locations may yield higher Ti values. High Ti concentrations in grain boundary regions have been excluded from the data set. The smallest grain sizes that can yield reliable Ti content are ~10–15 μm, which is within the size range of the smallest dynamically recrystallized grains in ultramylonites (Figures 7f and 8c).

[44] Average Ti concentrations in quartz do not show systematic variations in the three different microstructural domains and are always greater than 100 ppm, yielding peak temperatures of 760°C–780°C at a TiO_2 activity of 0.7 and 800°C–820°C at a TiO_2 activity of 0.5 (Table 3). These estimates correspond well with the temperature obtained

Figure 9. (a–c) Results of P-T pseudosection analysis of leucosome-poor domain. Molar ratios of element oxide in TiNCKFMASH system are given at the bottom of Figure 9c. P-T phase topologies computed using the bulk rock composition of the leucosome-poor domain is shown in Figure 9a. The isopleths of garnet (prp and grs) are shown in Figure 9b. The symbols are explained below Figure 9c. The P-T conditions of the observed assemblage are indicated by the vertical hatched area in Figure 9b. The modal abundance of melt (vol %) is shown in Figure 9c. The white line in Figure 9c shows the range of temperature obtained from titanium-in-quartz thermometry, while the black dots represent the average temperature (°C) calculated for activities of TiO_2 of 1, 0.7, 0.5, left to right, respectively. For detailed documentation see Tables 1, 2, and 3. Mineral abbreviations are after Kretz [1983].

Table 1. Whole Rock XRF Analysis of Different Domains of Sample Ø15

	Leucosome-Poor Domain	Leucosome-Rich Domain
SiO_2	66.04	66.05
Al_2O_3	16.13	15.9
Fe_2O_3	6.22	4.39
MnO	0.04	0.06
MgO	4.13	4.28
CaO	2.38	2.49
Na_2O	1.37	1.45
K_2O	1.86	3.22
TiO_2	0.13	0.22
P_2O_5	0.09	0.11
Total	98.39	98.17
H_2O	1.61	1.83

from the thermodynamic modeling (Figure 9), and allow the deformation temperature to be determined between 760°C and 820°C.

[45] Another potential estimate of the temperature of deformation may be provided by the titanium-in-biotite geothermometer [*Henry et al.*, 2005]. However, this thermometer has only been calibrated for pressures from 0.3 to 0.6 GPa, whereas the Bardineset rocks were deformed at 0.75–0.95 GPa. Therefore, the titanium-in-biotite thermometer was not applied in this study.

4.5. FTIR Measurements

[46] The aim of the FTIR measurements was to determine the intracrystalline water content within individual quartz grains in the leucosome-rich and leucosome-poor domains. Therefore, the analyses were carried out on optically clear regions of quartz grains, with a squared aperture of 50 × 50 μm, in order to exclude grain boundaries, cracks, and optically visible fluid inclusions. Given the section thickness of ~167 μm the analysis will yield an intracrystalline water content for individual grain sizes of ~200 μm. Below this size, a contribution of H_2O in the grain boundary region has to be expected. The average grain size of quartz in the leucosome-rich domain is larger than the thickness and the size of most of the quartz grains in the leucosome-poor domains is on the same order of magnitude as in the measured region. Thus, the H_2O content of the grain boundary region could have contributed to the measured total H_2O. However, care was taken to perform measurements on selected crystals larger that the section thickness in order to probe only the core volume of the crystals. Absence of grain boundaries was checked by moving the focus of the microscope through the samples. The average grain size in the ultramylonite layers is much smaller and, therefore, the ultramylonites have not been measured.

[47] The broad peak from ~2800 to 3800 cm^{-1}, centered at ~3400 cm^{-1}, is attributed to molecular water defects, which are responsible for H_2O weakening in quartz [*Kronenberg et al.*, 1986; *Gerretsen et al.*, 1989; *Paterson*,

Table 2. Representative Mineral Chemical Analysis and Structural Formula of Garnet and Biotite[a]

	Garnet					Biotite				
	Leucosome-Poor Domain (N = 6)			Leucosome-Rich Domain (N = 4)		Inclusion in Garnet	Leucosome-Poor Domain (N = 4)		Leucosome-Rich Domain (N = 3)	
SiO_2	37.52	38.03	38.87	38.32	38.16	37	36.94	38.2	37.51	36.84
TiO_2	0.02	0	0.01	0.03	0.01	5.49	3.84	3.26	3.88	3.73
Al_2O_3	21.9	22.02	22.45	21.63	21.69	17.86	16.24	17.39	17.45	17.76
Cr_2O_3	0	0	0	0	0	0	0	0	0	0
Fe_2O_3[b]	2.58	2.82	2.05	2.74	2.83	0	0	0	0	0
FeO	26.06	25.63	25.55	27.83	27.56	9.53	15.34	10.75	12.64	13.06
MnO	0.48	0.47	0.46	0.51	0.66	0.03	0	0.03	0	0.05
MgO	9.02	9.54	9.87	8.55	8.45	16.23	12.91	16.43	14.31	14.72
CaO	1.75	1.75	2.21	1.68	1.69	0.02	0.41	0.05	0.05	0
Na_2O	0	0.03	0	0.01	0.04	0.07	0.13	0.11	0.09	0.07
K_2O	0.01	0	0.01	0.01	0	9.7	10.21	9.61	9.26	8.65
Totals	99.33	100.29	101.49	100.41	101.91	95.94	96.02	95.84	95.2	94.89
Oxygens	12	12	12	12	12	11	11	11	11	11
Si	2.919	2.923	2.941	2.942	2.937	2.672	2.754	2.767	2.757	2.716
Ti	0.001	0	0	0.002	0.001	0.298	0.215	0.178	0.214	0.207
Al	2.009	1.995	2.002	1.958	1.968	1.521	1.428	1.485	1.512	1.544
Cr	0	0	0	0	0	0	0	0	0	0
Fe_3[b]	0.151	0.163	0.117	0.158	0.164	0	0	0	0	0
Fe_2	1.696	1.648	1.617	1.787	1.773	0.576	0.957	0.651	0.777	0.805
Mn	0.032	0.031	0.03	0.033	0.043	0.002	0	0.002	0	0.003
Mg	1.046	1.093	1.113	0.978	0.969	1.747	1.435	1.774	1.567	1.617
Ca	0.146	0.144	0.179	0.138	0.139	0.002	0.032	0.004	0.004	0
Na	0	0.004	0	0.002	0.006	0.009	0.019	0.015	0.012	0.011
K	0	0	0.001	0.001	0	0.895	2.754	2.767	2.757	2.716
Sum	8	8	8		8	7.721	7.812	7.765	7.713	7.718
Prp (mol %)	36.22	37.89	38.26	0.34	0.34	75.20	59.99	73.15	66.85	66.76
Grs (mol %)	0.05	0.05	0.06	0.05	0.05					

[a]Computed using AX [*Holland and Powell*, 1998].
[b]Calculated from stoichiometry.

Table 3. Ti-in-Quartz Thermometry[a]

	Ti (ppm)	T (°C) aTiO$_2$ = 1	T (°C) aTiO$_2$ = 0.7	T (°C) aTiO$_2$ = 0.5
		Ultramylonite Layers		
Average	113.4	730.27	771.35	813.31
SD	37.72	37.10	40.20	43.50
N[b]	23			
		Leucosome-Poor Domain		
Average	116	735.19	776.65	819.02
SD	33.66	31.42	34.07	36.89
N	5			
		Leucosome-Rich Domain		
Average	101.6	719.41	759.57	800.55
SD	31.27	31.26	33.87	36.64
N	12			

[a]P = 0.85 GPa.
[b]Number of analyses.

1989; *Kronenberg*, 1994]. Therefore, the intracrystalline water content was calculated from the integral area under the broad peak from 2800 to 3800 cm^{-1} using the Lambert-Beer law with the calibration of *Kats* [1962], such that:

$$C = (0.812 \times A_i)/t, \qquad (1)$$

where C is the water concentration in the sample (H:10^{6}Si), A_i is the integrated absorbance (cm^{-1}), t is the thickness of the sample (cm) and 0.812 is the integral molar absorption coefficient (mol^{-1} cm^{-2}) determined by *Kats* [1962]. The water content in ppm by weight is derived by dividing the calculated water content (H:10^{6}Si) by a factor of 6.67. We used the calibration of *Kats* [1962] to compare our results with the wide database of measurements collected by *Kronenberg and Wolf* [1990] on naturally and experimentally deformed quartzites. The absolute values of the water content depend on the chosen IR calibration. For instance, when using the calibrations of *Stipp et al.* [2006], established for water inclusion-bearing quartzite, the water contents are higher by a factor of 2.3 (Table 4).

[48] The IR spectra of quartz grains in the leucosome-rich domain indicate a heterogeneous water content with an average of 46 ppm water, by weight. Most of the grains have a very low water content of <40 ppm and show a rather flat absorption band in the 2800–3800 cm^{-1} range. A few grains contain higher amounts of intracrystalline water (from 76 to 165 ppm) (Figure 10).

[49] The quartz grains in the leucosome-poor domain consistently exhibit flat IR spectra in the 2800–3800 cm^{-1} range, indicative of extremely low water contents (Figure 10). The majority of the measured grains have water contents <30 ppm, by weight, and the content never exceeds 62 ppm. The very low intragranular water contents of quartz from the Bardineset samples (and particularly of the grains in the leucosome-poor domain) are comparable to the 30 ppm measured in a dry Brazil quartz by *Kronenberg et al.* [1986] and to the 40 ppm measured by *Nakashima et al.* [1995] in a granulite facies Archean metachert.

5. Discussion

5.1. Dominant Deformation Mechanism in Quartz

[50] The quartz microstructures clearly indicate that dynamic recrystallization has produced medium to fine-grained aggregates (Figures 6–8) in all domains. The CPO is strong in coarse and fine-grained quartz (Figures 6–8), and the flattened and elongate shape of the grains indicates intracrystalline deformation. In addition, the lack of microstructures indicative of extensive phase mixing between quartz, feldspars, and sillimanite in the ultramylonites suggests that diffusion creep has not been the dominant deformation mechanism in the fine-grained layers. Thus, from the microstructure it can be unequivocally concluded that the dominant deformation mechanism in quartz aggregates was dislocation creep.

[51] Rotation recrystallization clearly contributed to the progressive grain size reduction of quartz during deformation, as evidenced by the development of core subgrains, which are larger than the bulges (Figure 7d) and of the same size of recrystallized grains in the mylonite (~40 to 80 μm). Complete dynamic recrystallization has taken place initially by grain boundary migration in coarse-grained quartz (Figures 6a and 6b) and by dominantly bulging recrystallization in the finer grained quartz of leucosome-poor domains and ultramylonites (Figures 7 and 8). The strongly serrated grain boundaries of quartz indicate extensive grain boundary migration on a small scale (Figures 6a, 6b, 7a, and 8a). The c axis CPO does not change significantly with decreasing grain size from the leucosome-rich domain to the ultramylonite layers, and is consistent with the dominant activity of basal ⟨a⟩ slip system during dislocation creep and dynamic recrystallization (Figures 6c, 7e, and 8b).

5.2. Temperature and Pressure of Deformation

[52] The temperatures determined by the thermodynamic modeling and by TitaniQ thermometer all are in a fairly narrow range (760°C–820°C; Table 3 and Figure 9). All of the temperatures are determined from either synkinematic mineral assemblages or from dynamically recrystallized quartz grains, so that they are considered to be deformation temperatures. The pressures range from 0.75 to 0.95 GPa (Figure 9). Somewhat lower temperatures and pressures (700°C–750°C and 0.5 to 0.7 GPa) have been determined for these rocks by conventional thermobarometry by *Elvevold et al.* [1994].

[53] It is emphasized that there is no systematic difference in the deformation temperatures between leucosome-rich, leucosome-poor, and ultramylonite domains. In particular,

Table 4. Results of FTIR Measurements[a]

Analysis	Integrated Absorbance (cm−1)	*Kats* [1962] (H:10^6 Si)	*Kats* [1962] (ppm by weight)	*Stipp et al.* [2006] (H:10^6 Si)	*Stipp et al.* [2006] (ppm by weight)
		Leucosome-Rich Domain			
O15_LS0	2.988	145	22	338	51
O15_LS1	5.143	250	37	581	87
O15_LS2	22.607	1099	165	2555	383
O15_LS3	10.69	520	78	1208	181
O15_LS4	12.494	607	91	1412	212
O15_LS6	10.79	525	79	1220	183
O15_LS7	14.412	701	105	1629	244
O15_LS8	10.357	504	76	1171	176
O15_LS9	4.852	236	35	548	82
O15_LS10	0.105	5	1	12	2
O15_LS11	0.234	11	2	26	4
O15_LS12	2.768	135	20	313	47
O15_LS19	0.781	38	6	88	13
O15_LS22	0.514	25	4	58	9
O15_LS23	0.717	35	5	81	12
O15_LS24	1.405	68	10	159	24
		Leucosome-Poor Domain			
O15_HS0	2.718	132	20	307	46
O15_HS1	2.21	107	16	250	37
O15_HS2	0.233	11	2	26	4
O15_HS3	6.746	328	49	763	114
O15_HS4	4.527	220	33	512	77
O15_HS5	3.025	147	22	342	51
O15_HS7	8.523	414	62	963	144
O15_HS8	2.295	112	17	259	39
O15_HS9	2.054	100	15	232	35
O15_HS10	3.355	163	24	379	57
O15_HS11	2.838	138	21	321	48
O15_HS12	0.76	37	6	86	13
O15_HS13	6.556	319	48	741	111
O15_HS14	0.514	25	4	58	9
O15_HS15	3.608	175	26	408	61
O15_HS16	3.023	147	22	342	51
O15_HS17	4.54	221	33	513	77
O15_HS18	0.649	32	5	73	11
O15_HS19	1.025	50	7	116	17
O15_HS21	0.402	20	3	45	7

[a]Sample thickness = 0.0167 cm.

the deformation stage of localized shear zones associated with bulging recrystallization does not indicate different temperatures from those of the coarser-grained quartzitic migmatites. It can be concluded, as already pointed out by *Kohn and Northrup* [2009], that the TitaniQ thermometer records deformation temperatures well, provided that Ti exchange is rapid. The Ti exchange is likely to be complete during grain boundary migration, which is the principal mechanism in bulging recrystallization. The preservation of small sillimanite grains along the ultramylonite foliation (Figures 5d and 8a) is also consistent with the high temperatures determined by TitaniQ. Thus, the fine-grained, dynamically recrystallized ultramylonite layers have formed during high temperature granulite facies deformation.

5.3. Quartz Grain Size

[54] The larger quartz grains commonly show bulges and recrystallization to small grains (Figures 7a–7d) that are transitional to fine-grained ultramylonite shear zones, where the grain size is very small (11–17 μm) given the high T conditions of the Bardineset deformed migmatites. Flow stresses of ~75 to 100 MPa, derived from recrystallized grain size piezometry, have been reported for low T, greenschist

facies quartz-rich mylonites [e.g., *Stipp et al.*, 2002, 2010; *Menegon et al.*, 2011], but, so far, not for granulite facies rocks. The stresses obtained from the *Stipp and Tullis* [2003] piezometer in the grain size range of 11 to 17 μm are determined for experimentally recrystallized grains in "regime 3" [*Hirth and Tullis*, 1992]. *Stipp et al.* [2010] conclude that the grain boundary migration recrystallization observed in natural rocks, which commonly has been correlated with regime 3 of experimental samples [*Stipp et al.*, 2002], is not attainable experimentally. This situation and the fact that the Bardineset rocks are dry (see below) may render the stress determination somewhat inaccurate, but, semiquantitatively, there can be no doubt that the small grain sizes in dynamically recrystallized rocks indicate high stresses during dislocation creep deformation.

[55] There is clear evidence for overprinting of the bulging recrystallization microstructures over the earlier, coarse-grained, grain boundary migration recrystallization microstructures (Figures 6b, 7b, and 7c). The overprinting indicates that the localization of deformation in narrow shear zones took place at increased stresses, still at granulite facies P, T conditions and subsequent to shearing, which produced the lower stress, coarse-grained microstructures.
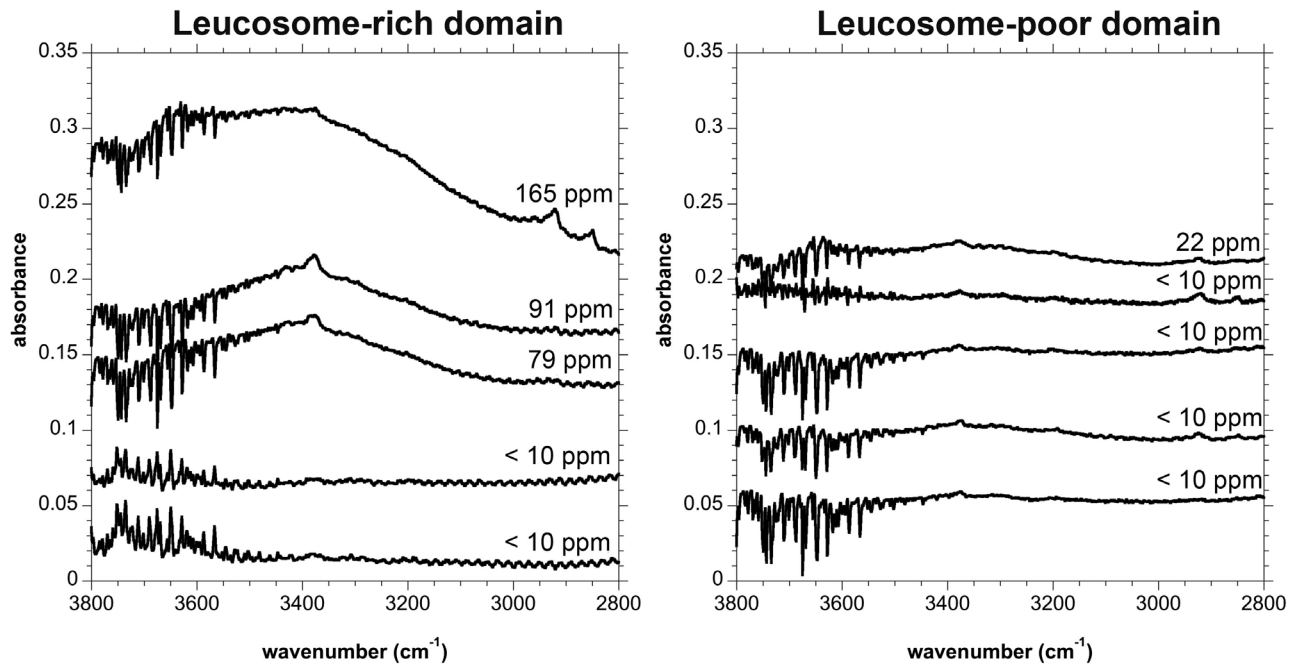
Figure 10. Representative FTIR absorption spectra of individual quartz grains from the leucosome-rich and leucosome-poor domains. Spectra are plotted with an offset for clarity. For detailed documentation see Table 4.

5.4. The Effect of Intracrystalline Water Content on Quartz Microstructures and Strength

[56] The intracrystalline water content of quartz from the Bardineset leucosome-poor domains is very low, less than 10 ppm in most cases and 22 ppm on average (Figure 10). These contents are on the same order as dry Brazil quartz, which has been used in rock-deformation experiments. Dry Brazil quartz, with intracrystalline water content typically less than 40 ppm, shows extremely high plastic yield strength, on the order of 2.0–3.0 GPa even at temperatures of 1000°C [e.g., *Griggs and Blacic*, 1965; *Blacic and Christie*, 1984; *Kronenberg et al.*, 1986]. On the contrary, quartzite samples commonly used in rock-deformation experiments usually contain well above 200 ppm of water [e.g., *Kronenberg and Wolf*, 1990; *Stipp et al.*, 2006] and can be deformed plastically up to high strains at low flow stresses in a solid-medium apparatus [e.g., *Tullis et al.*, 1973; *Kronenberg and Tullis*, 1984; *Tullis and Yund*, 1989; *Post and Tullis*, 1998]. The water content of such quartzites used as starting material is similar to those measured in many natural, quartz-rich mylonites deformed under greenschist to amphibolite facies conditions [*Kronenberg and Wolf*, 1990, and references therein; *Nakashima et al.*, 1995; *Gleason and DeSisto*, 2008]. It is inferred here that the high flow stresses determined in the Bardineset ultramylonites (at high temperatures of deformation) are caused by the fact that the quartz was "dry" during the deformation process.

[57] Recrystallized grain size piezometers calibrated in the laboratory use quartz with higher water contents as starting material (e.g., 113–280 ppm H_2O in the work by *Stipp et al.* [2006] as calculated with the *Kats* [1962] calibration) and, therefore, yield differential stress values that might not be accurate for dry quartz (e.g., for quartz containing <50 ppm H_2O). Piezometry is applicable to dry quartz, because the dislocation density versus stress relationship and inverse grain (or subgrain) size versus stress relationship are effective in dislocation creep deformation [e.g., *Poirier*, 1985], but the exact quantification of the relationship does not exist, so far, and could be somewhat different from wet quartz. As this uncertainty cannot be resolved at this stage, the differential stresses estimated for the Bardineset quartz mylonites have to be considered with some caution, but, regardless of whether the values are very accurate or not, it is safe to state that the flow stress certainly was considerably higher than those of the coarser-grained quartz outside of the fine-grained ultramylonites.

[58] Under the conditions of higher water content, the extrapolation of dislocation creep flow laws for wet quartz has yielded good results in the assessment of strength and strain rate in cases of natural deformation [e.g., *Hirth et al.*, 2001; *Stipp et al.*, 2002; *Jeřábek et al.*, 2007; *Mancktelow and Pennacchioni*, 2010]. In order to compare the strength relationships of wet and dry quartz at the high temperatures of deformation, we use dislocation creep flow laws for quartz to evaluate the mechanical behavior of the deformed migmatitic gneisses. In this comparison, the stress values of ultramylonites have been used as determined, notwithstanding the potential problem of piezometry applicability to dry quartz discussed above. Figure 11 displays the extrapolation of dislocation creep flow laws for wet quartz to natural strain rates of 10^{-12} and 10^{-14} s^{-1} at T > 600°C. We have used the experimental calibrations carried out by *Luan and Paterson* [1992] and *Rutter and Brodie* [2004] in the gas apparatus as well as the ones by *Gleason and Tullis* [1995] in the molten salt cell in a Griggs-type apparatus, both under melt-present and melt-absent conditions. In
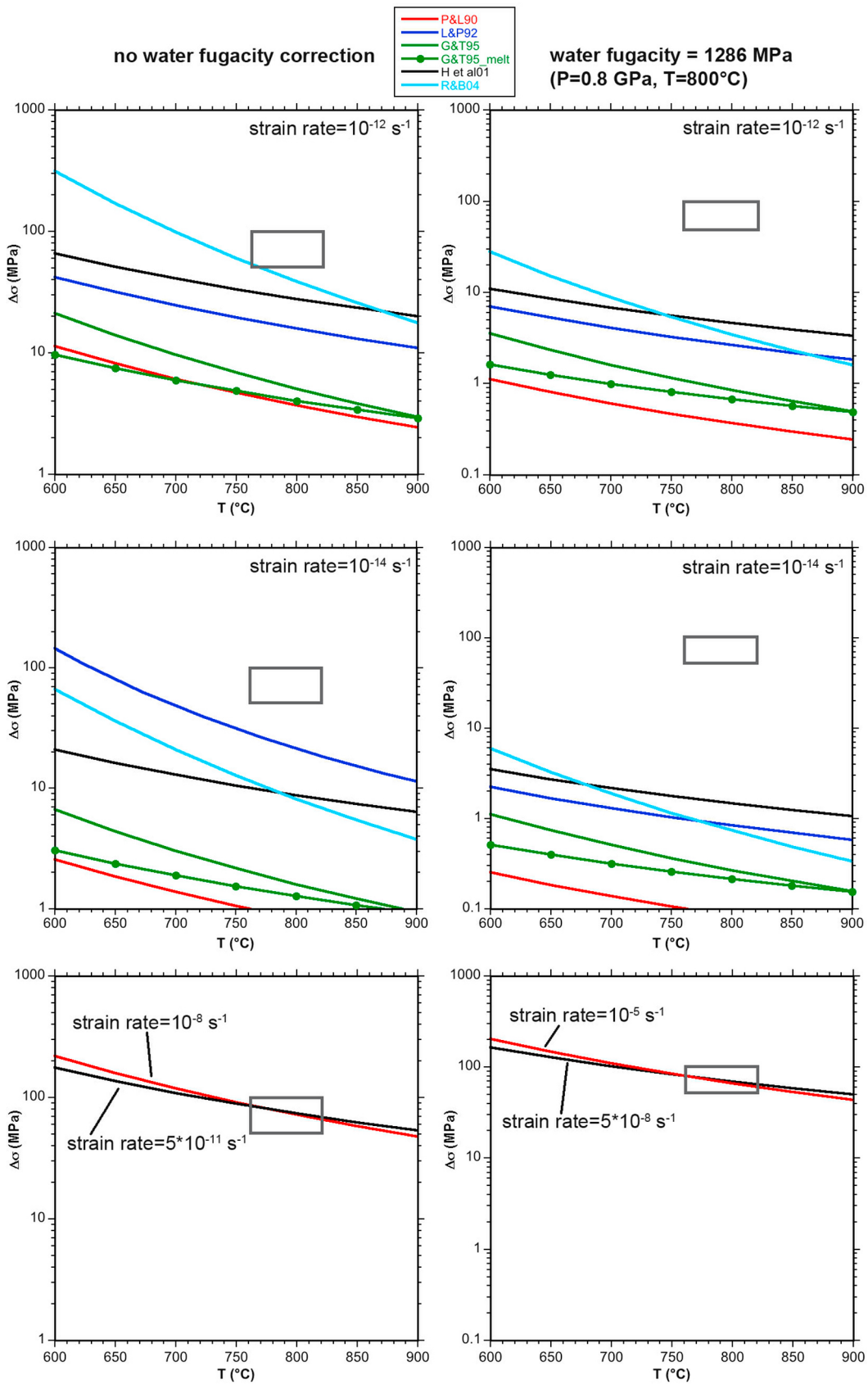
Figure 11

Table 5. Coefficients of the Dislocation Creep Flow Laws for Wet Quartz Used in This Study

Flow Law	A (MPa^{-n} s^{-1})	m[a]	Q (kJ mol^{-1})	n
Paterson and Luan [1990]	6.5×10^{-8}	n.d.	135	3.1
Luan and Paterson [1992]	4×10^{-10}	n.d.	152	4
Gleason and Tullis [1995]	1.1×10^{-4}	1	223	4
Gleason and Tullis [1995], with melt	1.8×10^{-8}	1	137	4
Hirth et al. [2001]	6.30957×10^{-12}	1	135	4
Rutter and Brodie [2004]	$10^{-4.93}$	1	242	2.97

[a]In the calculation results shown in Figure 11 we used $m = 1$ for the *Paterson and Luan* [1990] and *Luan and Paterson* [1992] flow laws even though the dependence of strain rate on water fugacity was not determined in those studies.

addition, we considered the theoretical flow laws of *Paterson and Luan* [1990] and *Hirth et al.* [2001], both derived from the integration of experimental and natural data (Table 5).

[59] The rheology of quartz deforming by dislocation creep is generally described in terms of a power law equation:

$$\dot{\varepsilon} = A f_{H_2O}^m e^{(-Q/RT)} \sigma^n, \qquad (2)$$

with the stress exponent n ranging from 2.97 to 4 for the flow laws used in this study. A linear dependence of strain rate on the water fugacity was consistently derived for the flow laws considered here, although the actual mechanism of water fugacity on the creep strength of quartz is still poorly established. We therefore present the extrapolation of dislocation creep flow laws for quartz both with and without the water fugacity correction (Figure 11). A water fugacity of 1286 MPa is calculated from the water fugacity coefficient reported by *Tödheide* [1972] at T = 800°C, P = 0.8 GPa. Also indicated in Figure 11 is the range of temperature and stress conditions in the Bardineset area, as determined from pseudosection modeling, TitaniQ thermometry, and recrystallized grain size piezometer for quartz (T = 760°C–820°C, $\Delta\sigma$ = 50–100 MPa). It is evident from Figure 11 that the stresses of the ultramylonite layers in the migmatitic gneisses are much higher than the predictions from the flow laws at geological strain rates of 10^{-12} to 10^{-14} s^{-1} (Figure 11). This is particularly dramatic when considering the water fugacity correction, but the effect is obvious even without accounting for it.

[60] The geologically constrained dislocation creep flow laws of *Paterson and Luan* [1990] and *Hirth et al.* [2001] for wet quartz yield meaningful results in the calculation of strain rate in naturally deformed quartzites [*Stipp et al.*, 2002]. However, if we consider the temperatures and stresses of deformation of the Bardineset area, the rock should have deformed at strain rates of 10^{-5} to 10^{-8} s^{-1} and 5×10^{-8} to 5×10^{-11} s^{-1} for differential stress of 50–100 MPa (Figure 11). The same high strain rates are

obtained from the recrystallization mechanism map of quartz proposed by *Stipp et al.* [2002]. At 750°C–800°C, recrystallization by a combination of bulging and subgrain rotation should take place at strain rates of 10^{-6} to 10^{-9} s^{-1}. These strain rates partly fall into the range of laboratory strain rates and are very unlikely. Instead, it is very likely that the strength of quartz was very high due to dry conditions during deformation, as indicated by the FTIR measurements.

[61] The dislocation creep flow law calibrated by *Rutter and Brodie* [2004] is the one that more closely approaches the quartz strength estimated from the grain size piezometry in the Bardineset area, for a geological strain rate of 10^{-12} s^{-1} (without accounting for the water fugacity correction; Figure 11). This flow law was obtained from deformation experiments performed on hot-pressed synthetic quartzite prepared from dry Brazilian quartz crystals, which are believed to have subsequently incorporated sufficient water during grain growth to become weaker than the starting dry quartz grains [*Rutter and Brodie*, 2004]. The comparison of this flow law with our results could potentially indicate that the quartz grains in the experiments, although partially hydrated, did not incorporate sufficient water. If this is correct, the dislocation creep flow law of *Rutter and Brodie* [2004] could perhaps be more appropriate for the description of the rheology of quartz under dryer conditions.

[62] A water-deficient environment during the development of ultrafine-grained quartz mylonites under amphibolite facies (T = 510°C–580°C, P = 0.25–0.45 GPa) metamorphic conditions was inferred by *Pennacchioni and Cesare* [1997] and *Fitz Gerald et al.* [2006]. The ultrafine quartz grains formed by subgrain rotation recrystallization at a flow stress of ~200 MPa, if the recrystallized grain size piezometer of *Stipp and Tullis* [2003] is used. *Fitz Gerald et al.* [2006] observed a very small amount of grain boundary porosity, suggestive of dry conditions during deformation, but water content was not measured. The conclusions of our study are consistent with those of *Fitz Gerald et al.* [2006] and extend them, because: (1) it is documented that high stress deformation of quartz has

Figure 11. Flow stress versus temperature plots calculated from the dislocation creep flow laws listed in Table 5 (P&L90, *Paterson and Luan* [1990]; L&P92, *Luan and Paterson* [1992]; G&T95, *Gleason and Tullis* [1995]; G&T95_melt, *Gleason and Tullis* [1995] with melt present; H *et al.*01, *Hirth et al.* [2001]; and R&B04, *Rutter and Brodie* [2004]). The plots in the left column are calculated without including a water fugacity correction. The plots in the right column include the water fugacity (1286 MPa) at a confining pressure of 0.80 GPa and fugacity exponent $m = 1$. The rectangle indicates the estimated temperature and stress conditions of the Bardineset quartzites (T = 760°C–820°C, $\Delta\sigma$ = 50–100 MPa). The two plots at the bottom show the strain rates at which the flow laws of *Paterson and Luan* [1990] and *Hirth et al.* [2001] match the deformation conditions of the Bardineset area.

taken place at an even higher metamorphic grade, and (2) it is confirmed by FTIR that the quartz is dry.

[63] The Bardineset samples show chessboard subgrains and crystallographic orientation suitable for prism ⟨c⟩ slip only in the leucosome-rich domain and not in the leucosome-poor domain (Figure 6). The occurrence of chessboard subgrains should indicate P, T conditions in the stability field of β-quartz [*Kruhl*, 1996], where prism ⟨c⟩ is expected to be the dominant slip system in quartz. The P, T conditions of deformation in the Bardineset area lie exactly across the quartz α-β transition [see *Groos and Van Heege*, 1973] and therefore we cannot rule out that the absence of chessboard subgrains in the mylonite and ultramylonite might reflect slight variations in the metamorphic P, T conditions with respect to those recorded by the leucosome-rich domain, although the TitaniQ thermometer yielded very constant results from the three microstructural domains of the rocks (Table 3). However, in many cases chessboard patterns have been reported from granitoids deforming near their solidus temperature in the presence of a melt phase [e.g., *Gapais and Barbarin*, 1986; *Zibra et al.*, 2010]. *Mainprice et al.* [1986] argue that the activity of prism ⟨c⟩ slip requires relatively wet environments. The leucosome-rich domains in the Bardineset samples satisfy both conditions, as they contain patches of deforming melt, and the water content is higher than in the leucosome-poor domain, as established from FTIR measurements, which document a higher total intracrystalline water content (although rather low in absolute terms) in quartz grains in the leucosome-rich domain (Figure 10). The higher water content in leusosome-rich domains is consistent with pseudosection calculations (1.26 wt % versus 0.69 wt %, Figure 9). A higher availability of water could therefore have favored the local activity of prism ⟨c⟩ slip in quartz grains in close proximity to the patches of leucosome, but not in the leucosome-poor, quartz-rich mylonites.

[64] In summary, our study indicates that the conditions typical of granulite facies metamorphism attained through dehydration melting and partial melt extraction are dry enough that the extrapolation of dislocation creep flow laws for wet quartz (and probably, in general, flow laws for wet minerals) does not describe the mechanical behavior of the lower crust accurately. Dry quartz under granulite facies conditions is strong and the use of dislocation creep flow laws for wet quartz will substantially underestimate the crustal strength.

5.5. Effect of Melt Presence on Deformation of Bardineset Migmatites

[65] In the Bardineset deformed migmatites, thermodynamic modeling (Figure 9) indicates that less than 5 vol % of melt was present during the deformation, and this volume percentage is observed from microgranitoid stringers with cuspate and lobate outlines (Figure 5a), monomineralic films of K-feldspar rimming sillimanite porphyroclasts (Figure 5b), and low apparent dihedral angles at the quartz-quartz-feldspar triple junctions (Figure 5f). The majority of the quartz grain boundaries are not wetted by melt films (Figures 5a–5e). The microgranitoid stringers in the quartzitic mylonite occur as isolated patches along the foliation, and do not form an interconnected weak layer microstructure (IWL) [*Handy*, 1994]. Also the irregular-shaped feldspar

pockets, films, and grains in the ultramylonite layers form isolated occurrences without contiguous layers.

[66] These observations suggest that the amount of melt was not sufficient to pervasively wet grain boundaries of the solid aggregate. There is no transition from a crystal framework containing isolated melt pockets to the formation of an interconnected network of layers of melt that may localize deformation [*Rosenberg and Handy*, 2005]. A minimum melt content of 7 vol % has been estimated for the transition to connected melt in felsic compositions [*Rosenberg and Handy*, 2005] and seems to be consistent with our observation of ~5% melt in isolated patches. We conclude that the solid phases of the Bardineset samples form a load-bearing framework (LBF) [*Handy*, 1994] of polycrystalline quartz, in which the weaker phase (melt stringers and melt films) occurs as isolated pockets. The deformation of such migmatites will be controlled by the solid framework and not by the melt layers.

[67] Experimental deformation of melt-bearing crustal rocks consistently indicates a reduction of rock strength with increasing melt fraction [e.g., *van der Molen and Paterson*, 1979; *Dell'Angelo and Tullis*, 1988; *Rutter et al.*, 2006]. The deformation mechanism associated with the melt-induced strength drop can be diffusion-accommodated granular flow, the primary reason for that being the ability of melt to enhance the diffusion rate [*Dell'Angelo et al.*, 1987; *Rosenberg and Handy*, 2001; *Rutter et al.*, 2006]. A melt-induced transition to dominant diffusion creep has been inferred to occur in naturally deformed rocks as well [*Rosenberg and Berger*, 2001]. Alternatively, the dominant deformation mechanism can be dislocation creep, as shown in experimentally [*Dell'Angelo et al.*, 1987; *Gleason and Tullis*, 1995] and naturally [*Berger and Kalt*, 1999; *Rosenberg and Riller*, 2000] deformed partially molten rocks. In the Bardineset migmatites, the dominant deformation mechanism is identified as dislocation creep in the solid quartz and is only indirectly affected by the partial melting (by producing a water-depleted assemblage).

5.6. Implications for the Strength of the Felsic Lower Crust

[68] Dehydration melting of biotite has been identified as the melt-forming reaction in the Bardineset samples. Once dehydration melting starts, the aqueous fluid fractionates into the silicate melt and may cause a dehydration of the adjacent rock. If the melt crystallizes in situ, the adjacent rocks are likely to be at least partially rehydrated, but if most of the melt is segregated and removed, the protolith will remain effectively dehydrated [e.g., *Brown*, 2002; *White and Powell*, 2002]. In the Bardineset samples, the leucosome-rich and leucosome-poor domains are interpreted to represent partially rehydrated and dehydrated rock, respectively. In agreement with this, FTIR measurements and pseudosection modeling indicate a higher water content in the leucosome-rich domain. The subsequent localization of deformation in fine-grained recrystallized quartzite aggregates at higher stresses took place in the dry leucosome-poor domain. From these data and observations it is inferred that the degree of melt segregation and removal determines the strength evolution of the deforming rock through the availability of water.

[69] The well-developed tectonic foliation of the Bardineset area and the stromatic character of the migmatites indicate that the melt segregation primarily occurred along the foliation and was aided by deformation [*Brown*, 1994; *Sawyer*, 2001]. Melt removal is accompanied by the progressive formation of a load-bearing framework of dry quartz crystals, where a small amount of melt (<5 vol %) is largely retained in isolated pockets. The progressive dehydration and hardening of quartz will induce an increase in flow stress during subsequent shearing, which is reflected in the formation of narrow shear zones, where the subgrain size is decreased and, eventually, bulging recrystallization develops much smaller recrystallized grains. *White and Powell* [2002] argued that melt loss might strongly affect the deformation properties of lower crustal rocks, presumably making them stronger than their melt-bearing equivalents. This study documents the effect of progressively strengthening quartz-rich rock by demonstrating the dry condition of residual quartz, which is stronger during subsequent deformation.

[70] In this context, it is interesting to note that small amounts (<5 vol %) of residual melt do not weaken dry restitic granulites, because the amount of melt is insufficient to wet the grain boundaries pervasively and to break down the solid phase framework. Instead, the effect of drying the residual solid phases by partial melting and melt segregation results in pronounced strengthening of the rock, which is evident from the subsequent deformation at higher stresses. The mechanism of potentially drying rocks by partial melting and melt segregation has been postulated for mantle rocks by *Karato* [1986] and for crustal rocks by *White and Powell* [2002].

[71] A radically different effect is expected in hydrous granitoid plutons deriving from extracted melt (which carries the dissolved water) and deforming during cooling near their solidus temperature in the presence of melt. Under such conditions, even small amounts of interstitial melts are commonly sufficient to pervasively wet the grain boundaries [*Rosenberg and Riller*, 2000] and potentially induce a transition to melt-enhanced diffusion creep and subsequent weakening [e.g., *Rosenberg and Berger*, 2001]. However, this situation does not apply to the restitic rocks analyzed in the present study.

[72] Given that dehydration melting reactions associated with melt removal are widely considered to be effective mechanisms for the formation of granulites [e.g., *White and Powell*, 2002; *Guernina and Sawyer*, 2003], the results of our study may be applied to large portions of felsic lower crust, which are likely to be dry and strong [e.g., *Maggi et al.*, 2000; *Jackson*, 2002; *Jackson et al.*, 2004]. In particular, dehydration and strengthening of the felsic lower continental crust induced by partial melting and melt loss can be a common mechanical evolution in intracontinental rift settings. The underplating of mantle-derived, dry large magmatic bodies associated with lithospheric thinning causes partial melting in the lower crust with the formation of dry residual granulites [*Sandiford and Powell*, 1986; *Bohlen and Mezger*, 1989; *Schuster and Stüwe*, 2008]. The lower crust becomes effectively dry and strong by this process, as shown for the Seiland Igneous Province.

[73] The strengthening effect proposed in this study is conceivably more pronounced in old, cratonic portions of the crust, which could have experienced multiple events of partial melting and dehydration during their geological evolution. This seems to be the case for the Eidvågeid gneisses (possibly the protolith of the Bardineset migmatite), which underwent migmatitization prior to the intrusion of the Seiland Igneous Province at 570–520 Ma [*Rice*, 1990; *Corfu et al.*, 2007]. In the light of this observation, it is worth noting that *Nakashima et al.* [1995] reported an intracrystalline water content of 40 ppm in quartz grains from granulite facies Archean metacherts, which therefore are expected to show a similar rheological behavior as the Bardineset samples.

6. Conclusions

[74] The felsic granulite gneisses of Bardineset (Seiland Igneous Province, northern Norway) were deformed during partial melting, which occurred by biotite dehydration reactions. The heat source for the fluid-absent melting came from the intrusion of large gabbroic plutons at 570–520 Ma into the lower crust in an intracontinental rift setting [*Elvevold et al.*, 1994; *Roberts et al.*, 2006].

[75] There is direct evidence from microstructural observations, FTIR measurements, thermodynamic modeling, and Ti-in-quartz thermometry for dry quartz under granulite facies conditions (T = 760°C–820°C, P = 0.85 GPa). Quartz deformed at high differential stresses by dislocation creep and formed a load-bearing framework in a melt-poor migmatite, where ~5% melt was present but did not control the mechanical behavior, because it was located in isolated pockets. The high stress deformation of quartz occurred subsequent to an earlier, lower stress deformation, evidence for which is preserved particularly in the vicinity of segregated melt pockets.

[76] The melt distribution, water content and distribution, and overprinting relationships of quartz microstructures indicate a sequence of events where partial melting took place by biotite dehydration during deformation by dislocation creep in quartz. Water fractionated into the segregating melt, which collected in certain parts of the rock in isolated pockets. In this way, parts of the rock where melt was removed became dry and thereby mechanically stronger. The dry rock can only deform at high stresses, which are indicated by the small recrystallized grain size observed in localized shear zones and ultramylonites.

[77] Melt removal at a larger scale will result in a lower crust which is dry enough to be mechanically strong. The application of flow laws derived for wet quartz is not appropriate to estimate the behavior of such granulite facies parts of the lower crust. It is likely that this conclusion applies to other mineral flow laws as well.

References

Adams, B. L., S. I. Wright, and K. Kunze (1992), Orientation imaging: The emergence of a new microscopy, *Metall. Mater. Trans. A*, 24, 819–831, doi:10.1007/BF02656503.

Afonso, J. C., and G. Ranalli (2004), Crustal and mantle strengths in continental lithosphere: Is the jelly sandwich model obsolete?, *Tectonophysics*, 394, 221–232, doi:10.1016/j.tecto.2004.08.006.

Austrheim, H., and T. M. Boundy (1994), Pseudotachylytes generated during seismic faulting and eclogitization of the deep crust, *Science*, 265, 82–83, doi:10.1126/science.265.5168.82.

Berger, A., and A. Kalt (1999), Structures and melt fractions as indicators of rheology in cordierite-bearing migmatites of the Bayerische Wald (Variscan Belt, Germany), *J. Petrol.*, 40, 1699–1719, doi:10.1093/petroj/40.11.1699.

Blacic, J. D., and J. M. Christie (1984), Plasticity and hydrolytic weakening of quartz single crystals, *J. Geophys. Res.*, 89, 4223–4239, doi:10.1029/JB089iB06p04223.

Bohlen, S. R., and K. Mezger (1989), Origin of granulite terranes and the formation of the lowermost continental crust, *Science*, 244, 326–329, doi:10.1126/science.244.4902.326.

Brown, M. (1994), The generation, segregation, ascent and emplacement of granite magma: The migmatite-to-crustally-derived granite connection in thickened orogens, *Earth Sci. Rev.*, 36, 83–130, doi:10.1016/0012-8252(94)90009-4.

Brown, M. (2002), Retrograde processes in migmatites and granulites revised, *J. Metamorph. Geol.*, 20, 25–40, doi:10.1046/j.0263-4929.2001.00362.x.

Bürgmann, R., and G. Dresen (2008), Rheology of the lower crust and upper mantle: Evidence from rock mechanics, geodesy, and field observations, *Annu. Rev. Earth Planet. Sci.*, 36, 531–567, doi:10.1146/annurev.earth.36.031207.124326.

Connolly, J. A. D. (2005), Computation of phase equilibria by linear programming: A tool for geodynamic modeling and its application to subduction zone decarbonation, *Earth Planet. Sci. Lett.*, 236, 524–541, doi:10.1016/j.epsl.2005.04.033.

Corfu, F., R. J. Roberts, T. H. Torsvik, L. D. Ashwal, and D. M. Ramsay (2007), Peri-Gondwanan elements in the Caledonian nappes of Finnmark, northern Norway: Implications for the paleogeographic framework of the Scandinavian Caledonides, *Am. J. Sci.*, 307, 434–458, doi:10.2475/02.2007.05.

Dell'Angelo, L. N., and J. Tullis (1988), Experimental deformation of partially melted granitic aggregates, *J. Metamorph. Geol.*, 6, 495–515, doi:10.1111/j.1525-1314.1988.tb00436.x.

Dell'Angelo, L. N., J. Tullis, and R. A. Yund (1987), Transition from dislocation creep to melt-enhanced diffusion creep in fine-grained granitic aggregates, *Tectonophysics*, 139, 325–332, doi:10.1016/0040-1951(87)90107-7.

Elvevold, S., H. Reginiussen, E. J. Krogh, and F. Bjørklund (1994), Reworking of deep-seated gabbros and associated contact metamorphosed paragneisses in the southeastern part of the Seiland Igneous Province, northern Norway, *J. Metamorph. Geol.*, 12, 539–556, doi:10.1111/j.1525-1314.1994.tb00041.x.

Fitz Gerald, J. D., N. S. Mancktelow, G. Pennacchioni, and K. Kunze (2006), Ultrafine-grained quartz mylonites from high-grade shear zones: Evidence for strong dry middle to lower crust, *Geology*, 34, 369–372, doi:10.1130/G22099.1.

Gapais, D., and B. Barbarin (1986), Quartz fabric transition in a cooling syntectonic granite (Hermitage Massif, France), *Tectonophysics*, 125, 357–370, doi:10.1016/0040-1951(86)90171-X.

Gardien, V., A. B. Thompson, and P. Ulmer (2000), Melting of biotite + plagioclase + quartz gneisses: The role of H_2O in the stability of amphibole, *J. Petrol.*, 41, 651–666, doi:10.1093/petrology/41.5.651.

Gerretsen, J., M. S. Paterson, and A. C. McLaren (1989), The uptake and solubility of water in quartz at elevated pressure and temperature, *Phys. Chem. Miner.*, 16, 334–342, doi:10.1007/BF00199553.

Ghent, E. D., and M. Z. Stout (1984), TiO_2 activity in metamorphosed pelitic and basic rocks: Principles and applications to metamorphism in southeastern Canadian Cordillera, *Contrib. Mineral. Petrol.*, 86, 248–255, doi:10.1007/BF00373670.

Gleason, G. C., and S. DeSisto (2008), A natural example of crystal-plastic deformation enhancing the incorporation of water into quartz, *Tectonophysics*, 446, 16–30, doi:10.1016/j.tecto.2007.09.006.

Gleason, G. C., and J. Tullis (1995), A flow law for dislocation creep of quartz aggregates determined with the molten salt cell, *Tectonophysics*, 247, 1–23, doi:10.1016/0040-1951(95)00011-B.

Griggs, D. T., and J. D. Blacic (1965), Quartz: Anomalous weakness of synthetic crystals, *Science*, 147, 292–295, doi:10.1126/science.147.3655.292.

Groos, A. F. K., and J. P. T. Van Heege (1973), The high-low quartz transition up to 10 kb pressure, *J. Geol.*, 81, 717–724.

Guernina, S., and E. W. Sawyer (2003), Large-scale melt-depletion in granulite terranes: An example from the Archean Ashuanipi Subprovince of Quebec, *J. Metamorph. Geol.*, 21, 181–201, doi:10.1046/j.1525-1314.2003.00436.x.

Hacker, B. R., E. Gnos, L. Ratschbacher, M. Grove, M. McWilliams, S. V. Sobolev, J. Wan, and W. Zhenhan (2000), Hot and dry deep crustal xenoliths from Tibet, *Science*, 287, 2463–2466, doi:10.1126/science.287.5462.2463.

Handy, M. R. (1994), Flow laws for rocks containing two non-linear viscous phases: A phenomenological approach, *J. Struct. Geol.*, 16, 287–301, doi:10.1016/0191-8141(94)90035-3.

Handy, M. R., and J.-P. Brun (2004), Seismicity, structure and strength of the continental lithosphere, *Earth Planet. Sci. Lett.*, 223, 427–441, doi:10.1016/j.epsl.2004.04.021.

Heilbronner, R. (2000), Automatic grain boundary detection and grain size analysis using polarization micrographs or orientation images, *J. Struct. Geol.*, 22, 969–981, doi:10.1016/S0191-8141(00)00014-6.

Henry, D. J., C. V. Guidotti, and J. A. Thomson (2005), The Ti-saturation surface for low-to-medium pressure metapelitic biotite: Implications for geothermometry and Ti-substitution mechanisms, *Am. Mineral.*, 90, 316–328, doi:10.2138/am.2005.1498.

Hirth, G., and J. Tullis (1992), Dislocation creep regimes in quartz aggregates, *J. Struct. Geol.*, 14, 145–159, doi:10.1016/0191-8141(92)90053-Y.

Hirth, G., C. Teyssier, and W. J. Dunlap (2001), An evaluation of quartzite flow laws based on comparisons between experimentally and naturally deformed rocks, *Int. J. Earth Sci.*, 90, 77–87, doi:10.1007/s005310000152.

Holland, T. J. B., and R. Powell (1998), An internally consistent thermodynamic dataset for phases of petrological interest, *J. Metamorph. Geol.*, 16, 309–343, doi:10.1111/j.1525-1314.1998.00140.x.

Holness, M. B., and J. D. Clemens (1999), Partial melting of the Appin Quartzite driven by fracture-controlled H_2O infiltration in the aureole of the Ballachulish Igneous Complex, Scottish Highlands, *Contrib. Mineral. Petrol.*, 136, 154–168, doi:10.1007/s004100050529.

Holness, M. B., and E. W. Sawyer (2008), On the pseudomorphing of melt-filled pores during the crystallization of migmatites, *J. Petrol.*, 49, 1343–1363, doi:10.1093/petrology/egn028.

Holyoke, C. W., III, and A. K. Kronenberg (2010), Accurate differential stress measurement using the molten salt cell and solid salt assemblies in the Griggs apparatus with applications to strength, piezometers and rheology, *Tectonophysics*, 494, 17–31, doi:10.1016/j.tecto.2010.08.001.

Jackson, J. A. (2002), Strength of the continental lithosphere: Time to abandon the jelly sandwich?, *GSA Today*, 12, 4–10, doi:10.1130/1052-5173(2002)012<0004:SOTCLT>2.0.CO;2.

Jackson, J. A., H. Austrheim, D. McKenzie, and K. Priestley (2004), Metastability, mechanical strength, and the support of mountain belts, *Geology*, 32, 625–628, doi:10.1130/G20397.1.

Jackson, J. A., D. McKenzie, K. Priestley, and B. Emmerson (2008), New views on the structure and rheology of the lithosphere, *J. Geol. Soc.*, 165, 453–465, doi:10.1144/0016-76492007-109.

Jeřábek, P., H. Stünitz, R. Heilbronner, O. Lexa, and K. Schulmann (2007), Microstructural-deformation record of an orogen-parallel extension in the Vepor Unit, West Carpathians, *J. Struct. Geol.*, 29, 1722–1743, doi:10.1016/j.jsg.2007.09.002.

Karato, S. (1986), Does partial melting reduce the creep strength of the upper mantle?, *Nature*, 319, 309–310, doi:10.1038/319309a0.

Kats, A. (1962), Hydrogen in alpha quartz, *Philips Res. Rep.*, 17, 1–31; 133–195; 201–279.

Kirkland, C. L., J. S. Day, and M. J. Whitehouse (2008), Basement-cover relationships of the Kalak Nappe Complex, Arctic Norwegian Caledonides and constraints on Neoproterozoic terrane assembly in the North Atlantic region, *Precambrian Res.*, 160, 245–276, doi:10.1016/j.precamres.2007.07.006.

Kohlstedt, D. L., B. Evans, and S. J. Mackwell (1995), Strength of the lithosphere: Constraints imposed by laboratory experiments, *J. Geophys. Res.*, 100, 17,587–17,602, doi:10.1029/95JB01460.

Kohn, M. J., and C. J. Northrup (2009), Taking mylonites' temperatures, *Geology*, 37, 47–50, doi:10.1130/G25081A.1.

Kretz, R. (1983), Symbols for rock-forming minerals, *Am. Mineral.*, 68, 277–279.

Krill, A. G., and K. B. Zwaan (1987), Reinterpretation of Finnmarkian deformation on western Sørøy, northern Norway, *Nor. Geol. Tidsskr.*, 67, 15–24.

Kronenberg, A. K. (1994), Hydrogen speciation and chemical weakening of quartz, in *Silica: Physical Behavior, Geochemistry and Materials Applications*, edited by P. J. Heaney et al., *Rev. Mineral. Mineral. Soc. Am.*, 29, 123–176.

Kronenberg, A. K., and J. Tullis (1984), Flow strength of quartz aggregates: Grain-size and pressure effects due to hydrolytic weakening, *J. Geophys. Res.*, 89, 4281–4297, doi:10.1029/JB089iB06p04281.

Kronenberg, A. K., and G. H. Wolf (1990), Fourier transform infrared spectroscopy determinations of intragranular water content in quartz-bearing rocks: Implications for hydrolytic weakening in the laboratory and within the Earth, *Tectonophysics*, *172*, 255–271, doi:10.1016/0040-1951(90)90034-6.

Kronenberg, A. K., S. H. Kirby, R. D. Aines, and G. R. Rossman (1986), Solubility and diffusional uptake of hydrogen in quartz at high water pressures: Implications for hydrolytic weakening, *J. Geophys. Res.*, *91*, 12,723–12,744, doi:10.1029/JB091iB12p12723.

Kruhl, J. H. (1996), Prism- and basal-plane parallel subgrain boundaries in quartz: A microstructural geothermobarometer, *J. Metamorph. Geol.*, *14*, 581–589, doi:10.1046/j.1525-1314.1996.00413.x.

Le Breton, N., and A. B. Thompson (1988), Fluid-absent (dehydration) melting of biotite in metapelites in the early stages of crustal anatexis, *Contrib. Mineral. Petrol.*, *99*, 226–237, doi:10.1007/BF00371463.

Luan, F. C., and M. S. Paterson (1992), Preparation and deformation of synthetic aggregates of quartz, *J. Geophys. Res.*, *97*, 301–320, doi:10.1029/91JB01748.

Lund, M. G., H. Austrheim, and M. Erambert (2004), Earthquakes in the deep continental crust – Insights from studies on exhumed high-pressure rocks, *Geophys. J. Int.*, *158*, 569–576, doi:10.1111/j.1365-246X.2004.02368.x.

Maggi, A., J. A. Jackson, D. McKenzie, and D. Priestley (2000), Earthquake focal depths, effective elastic thickness, and the strength of the continental lithosphere, *Geology*, *28*, 495–498, doi:10.1130/0091-7613 (2000)28<495:EFDEET>2.0.CO;2.

Mainprice, D., J.-L. Bouchez, P. Blumenfeld, and J. M. Tubià (1986), Dominant *c* slip in naturally deformed quartz: Implications for dramatic plastic softening at high temperature, *Geology*, *14*, 819–822, doi:10.1130/0091-7613(1986)14<819:DCSIND>2.0.CO;2.

Mancktelow, N. S., and G. Pennacchioni (2010), Why calcite can be stronger than quartz, *J. Geophys. Res.*, *115*, B01402, doi:10.1029/2009JB006526.

Marchildon, N., and M. Brown (2002), Grain-scale melt distribution in two contact aureole rocks: Implications for controls on melt localization and deformation, *J. Metamorph. Geol.*, *20*, 381–396, doi:10.1046/j.1525-1314.2002.00376.x.

Menegon, L., S. Piazolo, and G. Pennacchioni (2011), The effect of Dauphiné twinning on plastic strain in quartz, *Contrib. Mineral. Petrol.*, *161*, 635–652, doi:10.1007/s00410-010-0554-7.

Müntener, O., J. Hermann, and V. Trommsdorff (2000), Cooling history and exhumation of lower-crustal granulite and upper mantle (Malenco, Eastern Central Alps), *J. Petrol.*, *41*, 175–200, doi:10.1093/petrology/41.2.175.

Nakashima, S., H. Matayoshi, T. Yuko, K. Michibayashi, T. Masuda, N. Kuroki, H. Yamagishi, Y. Ito, and A. Nakamura (1995), Infrared microspectroscopy analysis of water distribution in deformed and metamorphosed rocks, *Tectonophysics*, *245*, 263–276, doi:10.1016/0040-1951(94)00239-6.

Nasipuri, P., A. Bhattacharya, and S. Das (2009), Metamorphic reactions in dry and aluminous granulites: A Perple_X *P–T* pseudosection analysis of the influence of effective reaction volume, *Contrib. Mineral. Petrol.*, *157*, 301–311, doi:10.1007/s00410-008-0335-8.

Panozzo-Heilbronner, R., and C. Pauli (1993), Integrated spatial and orientation analysis of quartz *c*-axes by computer-aided microscopy, *J. Struct. Geol.*, *15*, 369–382, doi:10.1016/0191-8141(93)90133-U.

Paterson, M. S. (1989), The interaction of water with quartz and its influence in dislocation flow: An overview, in *Rheology of Solids and of the Earth*, edited by S.-I. Karato and M. Toriumi, pp. 107–142, Oxford Univ. Press, Oxford, U. K.

Paterson, M. S., and F. C. Luan (1990), Quartzite rheology under geological conditions, in *Deformation Mechanisms, Rheology and Tectonics*, edited by R. J. Knipe and E. H. Rutter, *Geol. Soc. Spec. Publ.*, *54*, 299–307.

Patino Douce, A. E., and S. J. Beard (1994), Dehydration-melting of biotite gneiss and quartz amphibolite from 3 to 15 kbar, *J. Petrol.*, *36*, 707–738, doi:10.1093/petrology/36.3.707.

Pennacchioni, G., and B. Cesare (1997), Ductile-brittle transition in pre-Alpine amphibolite facies mylonites during evolution from water-present to water-deficient conditions (Mont Mary Nappe, Italian Western Alps), *J. Metamorph. Geol.*, *15*, 777–791, doi:10.1111/j.1525-1314.1997.00055.x.

Poirier, J.-P. (1985), *Creep of Crystals: High-Temperature Deformation Processes in Metals, Ceramics, and Minerals*, Cambridge Univ. Press, Cambridge, U.K., doi:10.1017/CBO9780511564451.

Post, A., and J. Tullis (1998), The rate of water penetration in experimentally deformed quartzite; implications for hydrolytic weakening, *Tectonophysics*, *295*, 117–137, doi:10.1016/S0040-1951(98)00145-0.

Priestley, K., J. Jackson, and D. McKenzie (2008), Lithospheric structure and deep earthquakes beneath India, the Himalaya and southern Tibet, *Geophys. J. Int.*, *172*, 345–362, doi:10.1111/j.1365-246X.2007.03636.x.

Reginiussen, H., E. J. K. Ravna, and K. Berglund (1995), Mafic dykes from Øksfjord, Seiland Igneous Province, northern Norway: Geochemistry and palaeotectonic significance, *Geol. Mag.*, *132*, 667–681, doi:10.1017/S0016756800018902.

Rice, A. H. N. (1990), Possible basement rocks in the Kalak Nappe Complex on Sørøy, Finnmark, N. Norway, *Nor. Geol. Tidsskr.*, *70*, 159–172.

Roberts, D. (1973), Geologisk kart over Norge, berggrunnskart, Hammerfest 1:250000, map, Nor. Geol. Unders., Trondheim, Norway.

Roberts, R. J., F. Corfu, T. H. Torsvik, L. D. Ashwal, and D. M. Ramsay (2006), Short-lived mafic magmatism at 560–570 Ma in the northern Norwegian Caledonides: U-Pb zircon ages from the Seiland Igneous Province, *Geol. Mag.*, *143*, 887–903, doi:10.1017/S0016756806002512.

Rosenberg, C. L., and A. Berger (2001), Syntectonic melt pathways in granitic gneisses, and melt-induced transitions in deformation mechanisms, *Phys. Chem. Earth*, *26*, 287–293, doi:10.1016/S1464-1895(01)00058-8.

Rosenberg, C. L., and M. R. Handy (2001), Mechanism and orientation of melt segregation paths during pure shearing of a partially molten rock analogue (norcamphor-benzamide), *J. Struct. Geol.*, *23*, 1917–1932, doi:10.1016/S0191-8141(01)00037-2.

Rosenberg, C. L., and M. R. Handy (2005), Experimental deformation of partially melted granite revisited: Implications for the continental crust, *J. Metamorph. Geol.*, *23*, 19–28, doi:10.1111/j.1525-1314.2005.00555.x.

Rosenberg, C. L., and U. Riller (2000), Partial-melt topology in statically and dynamically recrystallized granite, *Geology*, *28*, 7–10, doi:10.1130/0091-7613(2000)28<7:PTISAD>2.0.CO;2.

Rudnick, R. L., and D. M. Fountain (1995), Nature and composition of the continental crust: A lower-crustal perspective, *Rev. Geophys.*, *33*, 267–309, doi:10.1029/95RG01302.

Rutter, E. H., and K. H. Brodie (2004), Experimental intracrystalline plastic flow in hot-pressed synthetic quartzite prepared from Brazilian quartz crystals, *J. Struct. Geol.*, *26*, 259–270, doi:10.1016/S0191-8141(03)00096-8.

Rutter, E. H., K. H. Brodie, and D. H. Irving (2006), Flow of synthetic, wet, partially molten "granite" under undrained conditions: An experimental study, *J. Geophys. Res.*, *111*, B06407, doi:10.1029/2005JB004257.

Rybacki, E., and G. Dresen (2000), Dislocation and diffusion creep of synthetic anorthite aggregates, *J. Geophys. Res.*, *105*, 26,017–26,036, doi:10.1029/2000JB900223.

Sandiford, M., and R. Powell (1986), Deep crustal metamorphism during continental extension: Modern and ancient examples, *Earth Planet. Sci. Lett.*, *79*, 151–158, doi:10.1016/0012-821X(86)90048-8.

Sawyer, E. W. (1999), Criteria for the recognition of partial melting, *Phys. Chem. Earth*, *24*, 269–279, doi:10.1016/S1464-1895(99)00029-0.

Sawyer, E. W. (2001), Melt segregation in the continental crust: Distribution and movement of melt in anatectic rocks, *J. Metamorph. Geol.*, *19*, 291–309, doi:10.1046/j.0263-4929.2000.00312.x.

Schuster, R., and K. Stüwe (2008), Permian metamorphic event in the Alps, *Geology*, *36*, 603–606, doi:10.1130/G24703A.1.

Shimizu, I. (2008), Theories and applicability of grain size piezometers: The role of dynamic recrystallization mechanisms, *J. Struct. Geol.*, *30*, 899–917, doi:10.1016/j.jsg.2008.03.004.

Stevens, G., and J. D. Clemens (1993), Fluid-absent melting and the role of fluids in the lithosphere: A slanted summary?, *Chem. Geol.*, *108*, 1–17, doi:10.1016/0009-2541(93)90314-9.

Stipp, M., and J. Tullis (2003), The recrystallized grain size piezometer for quartz, *Geophys. Res. Lett.*, *30*(21), 2088, doi:10.1029/2003GL018444.

Stipp, M., H. Stünitz, R. Heilbronner, and S. M. Schmid (2002), Dynamic recrystallization of quartz: Correlation between natural and experimental conditions, in *Deformation Mechanisms, Rheology and Tectonics: Current Status and Future Perspectives*, edited by S. De Meer et al., *Geol. Soc. Spec. Publ.*, *200*, 171–190.

Stipp, M., J. Tullis, and H. Behrens (2006), Effect of water on the dislocation creep microstructure and flow stress of quartz and implications for the recrystallized grain size piezometer, *J. Geophys. Res.*, *111*, B04201, doi:10.1029/2005JB003852.

Stipp, M., J. Tullis, M. Scherwath, and J. H. Behrmann (2010), A new perspective on paleopiezometry: Dynamically recrystallized grain size distributions indicate mechanism changes, *Geology*, *38*, 759–762, doi:10.1130/G31162.1.

Thomas, J. B., E. B. Watson, F. S. Spear, P. T. Shemella, S. K. Najak, and A. Lanzirotti (2010), TitaniQ under pressure: The effect of pressure and temperature on the solubility of Ti in quartz, *Contrib. Mineral. Petrol.*, *160*, 743–759, doi:10.1007/s00410-010-0505-3.

Thompson, J. B. (1959), Local equilibrium in metasomatic processes, in *Researches in Geochemistry*, edited by P. H. Abelson, pp. 427–457, Wiley, New York.

Tödheide, K. (1972), Water at high temperatures and pressures, in *Water: A Comprehensive Treatise*, vol. 1, edited by F. Franks, chap. 13, pp. 463–514, Springer, New York.

Tullis, J., and R. A. Yund (1989), Hydrolytic weakening of quartz aggregates: The effects of water and pressure on recovery, *Geophys. Res. Lett.*, *16*, 1343–1346, doi:10.1029/GL016i011p01343.

Tullis, J., J. M. Christie, and D. T. Griggs (1973), Microstructures and preferred orientations of experimentally deformed quartzites, *Geol. Soc. Am. Bull.*, *84*, 297–314, doi:10.1130/0016-7606(1973)84<297:MAPOOE> 2.0.CO;2.

van der Molen, I., and M. S. Paterson (1979), Experimental deformation of partially melted granite, *Contrib. Mineral. Petrol.*, *70*, 299–318, doi:10.1007/BF00375359.

Vernon, R. H. (1968), Microstructures of high-grade metamorphic rocks at Broken Hill, Australia, *J. Petrol.*, *9*, 1–22.

Wark, D. A., and E. B. Watson (2006), TitaniQ: A titanium-in-quartz geothermometer, *Contrib. Mineral. Petrol.*, *152*, 743–754, doi:10.1007/ s00410-006-0132-1.

White, R. W., and R. Powell (2002), Melt loss and the preservation of granulite facies mineral assemblages, *J. Metamorph. Geol.*, *20*, 621–632.

White, R. W., R. Powell, and T. J. B. Holland (2001), Calculation of partial melting equilibria in the system Na_2O-CaO-K_2O-FeO-MgO-Al_2O_3- SiO_2-H_2O (NCKFMASH), *J. Metamorph. Geol.*, *19*, 139–153, doi:10.1046/j.0263-4929.2000.00303.x.

White, R. W., R. Powell, and T. J. B. Holland (2007), Progress relating to calculation of partial melting equilibria for metapelites, *J. Metamorph. Geol.*, *25*, 511–527, doi:10.1111/j.1525-1314.2007.00711.x.

Yardley, B. W. D., and J. W. Valley (1994), How wet is the Earth's crust?, *Nature*, *371*, 205–206, doi:10.1038/371205a0.

Yardley, B. W. D., and J. W. Valley (1997), The petrologic case for a dry lower crust, *J. Geophys. Res.*, *102*, 12,173–12,185, doi:10.1029/ 97JB00508.

Zibra, I., J. H. Kruhl, and R. Braga (2010), Late Palaezoic deformation of post-Variscan lower crust: Shear zone widening due to strain localization during retrograde shearing, *Int. J. Earth Sci.*, *99*, 973–991, doi:10.1007/ s00531-009-0441-5.

H. Behrens, Institute of Mineralogy, University of Hannover, Callinstr. 3, D-30167 Hannover, Germany.

L. Menegon, P. Nasipuri, E. Ravna, and H. Stünitz, Department of Geology, University of Tromsø, Dramsveien 201, N-9037 Tromsø, Norway. (luca.menegon@uit.no)